Application of the Akaike Information Criterion to the interpretation of bender element tests

Guillaume Flood-Page, Luc Boutonnier, Jean-Michel Pereira

▶ **To cite this version:**

Guillaume Flood-Page, Luc Boutonnier, Jean-Michel Pereira. Application of the Akaike Information Criterion to the interpretation of bender element tests. Soil Dynamics and Earthquake Engineering, 2024, 177, pp.108373. 10.1016/j.soildyn.2023.108373 . hal-04391957

HAL Id: hal-04391957

https://hal.science/hal-04391957v1

Submitted on 12 Jan 2024

HAL is a multi-disciplinary open access archive for the deposit and dissemination of scientific research documents, whether they are published or not. The documents may come from teaching and research institutions in France or abroad, or from public or private research centers.

L'archive ouverte pluridisciplinaire **HAL**, est destinée au dépôt et à la diffusion de documents scientifiques de niveau recherche, publiés ou non, émanant des établissements d'enseignement et de recherche français ou étrangers, des laboratoires publics ou privés.

Distributed under a Creative Commons Attribution - NonCommercial - ShareAlike 4.0 International License

Graphical Abstract

Application of the Akaike Information Criterion to the interpretation of bender element tests

Guillaume Flood-Page, Luc Boutonnier, Jean-Michel Pereira

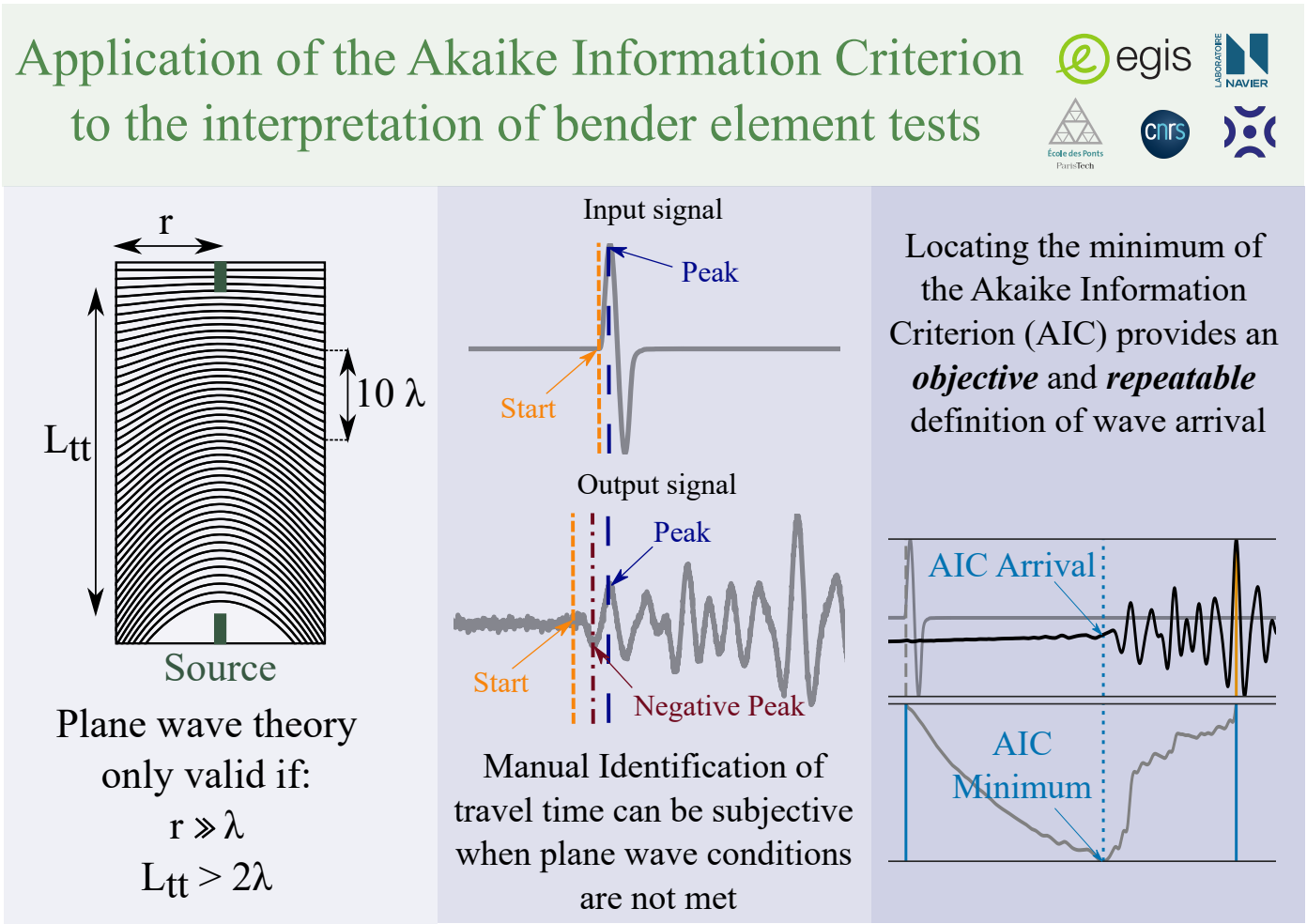

Application of the Akaike Information Criterion to the interpretation of bender element tests

Guillaume Flood-Page[a,b,*], Luc Boutonnier[a], Jean-Michel Pereira[b]

[a]*Egis, 3 rue du docteur Schweitzer, Seyssins, 38600, Auvergne-Rhone-Alpes, France*
[b]*Navier, Ecole des Ponts, Univ Gustave Eiffel, CNRS, Marne-la-Vallee, France*

Abstract

While the use of bender elements for geotechnical testing dates back to the sixties and seventies, the interpretation of this wave propagation test is still a debated topic. The most widely accepted method involves plotting a signal in the time domain and manually finding the arrival point. This requires identifying an arrival time corresponding to the velocity of a plane wave in a setting where the validity of plane wave theory is, at best, debatable. Inevitably, this manual interpretation process can become error-prone and subjective. While this paper does not pretend to solve the issue of applying plane wave theory outside its domain of validity, it mainly aims to make the interpretation process more objective and repeatable. To achieve this, a statistical tool named Akaike Information Criterion (AIC) is used to separate a signal into two stationary processes: before and after the arrival of a wave. The main challenge is to isolate a segment of signal where these two stationary processes can be identified. For this two separate algorithms are built using different methods of identifying the optimal signal segment. Both algorithms are described and tested on a large set of signals recorded on Fontainebleau sand specimens.

Keywords: Elasticity, Laboratory tests, Bender elements, AIC, Sands

Introduction

The use of piezo-electric sensors for measuring wave velocities at very small strains is, to our knowledge, first described in the work of Lawrence Jr (1965). Ceramic bender elements were later employed by Shirley and Hampton (1978) to measure shear wave velocities. Further developments on this design were proposed by Lings and Greening (2001) in order to measure both compression and shear waves velocities using a single set of bender-extender elements.

A more complete description of the evolution of bender element testing and interpretation can be found in the works of Lee and Santamarina (2005), Leong et al. (2005), Arroyo et al. (2006) or Alvarado and Coop (2012) among many others. Nevertheless, it is worth noting that while many different interpretation methods have been proposed, none has been unanimously accepted.

Fundamentally, most issues stem from two specific shortcomings of bender element testing. The first is the difference between the electrical input signal and the mechanical strain it induces in the piezo-electric element (Arroyo, 2007). The second is that the interpretation of the results relies on the application of plane wave propagation theory in an environment where its validity is often debatable. Theoretically, waves can be assumed to be plane if they are observed both in the *"far-field"*, far away from the source, and in an infinite medium (Achenbach, 1975). While the *far-field* criterion can be achieved in bender element testing if the propagation distance L_{tt} is several times greater than the wavelength (Sanchez-Salinero et al., 1986; Barrière et al., 2012), the medium can only be considered infinite for wavelengths much smaller than the radius of the specimen (Santamarina et al., 2001), condition that is rarely met when using a triaxial apparatus equipped with bender ele-

*Corresponding author: gfloodpage@gmail.com

ments.

While bender element tests are an extremely useful tool for observing the small-strain behaviour of soils, their interpretation is often made unreliable by the questionable applicability of plane wave theory. In conditions where this theory is not applicable, interpreting the test involves *"guessing"* which point of the recorded signal best corresponds to the arrival of a would-be plane wave. Although this manual process can be performed reliably, it is often fairly subjective, which limits the repeatability of the measurements. The Akaike Information Criterion, or *AIC*, (Akaike, 1998) is a statistical tool that has successfully been used to detect the arrival of both shear and compression waves in seismograms (Sleeman and van Eck, 1999; Zhang et al., 2003). Accordingly, this paper looks into the potential of *AIC* as a more objective criterion for detecting wave arrivals in bender-extender element tests. Although algorithms such as that described in Arroyo et al. (2003a) can already be used to improve the repeatability of manual arrival picking, personal experience has shown that such methods can struggle with complex signals. Notably, their application to the detection of compression wave arrival in gassy soils and of shear wave arrival in signals also containing compression waves did not yield satisfying results.

After a description of current bender element practice, the *AIC* is briefly introduced before describing two algorithms allowing the interpretation of bender element tests through this criterion. These algorithms are then verified on a set of P and S wave measurements performed on dry, gassy and saturated Fontainebleau sand.

1. Bender element interpretation

1.1. General considerations

As shown in Figure 1, bender-extender elements can be wired in two different ways (see the works of Lings and Greening, 2001 for details). The left-hand side setup in Figure 1 mostly generates compression waves while the right-hand one mainly emits shear waves. Unfortunately, they often actually generate both shear and compression waves. Bearing in mind the receiver is not always in the *far-field* (as is theoretically required by plane wave theory), the different wave components can get confused in the recorded signals. This issue, called *"near-field effect"*, is particularly sensitive when measuring shear wave velocity as reflected P waves can mask the arrival of the S waves.

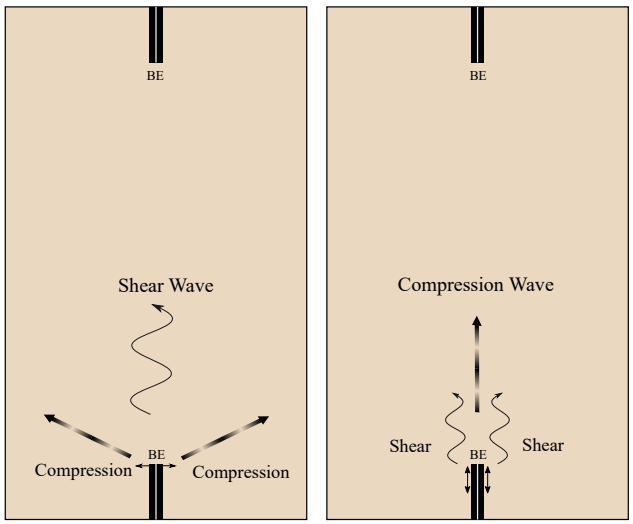

Figure 1: Generating P and S waves using bender elements. While it is possible to predominantly produce compression or shear waves, bender-extender elements inevitably produce both.

1.2. Traditional time domain methods

A majority of authors use time domain methods for interpreting bender element tests (e.g. Viggiani and Atkinson, 1995; Alvarado and Coop, 2012 among many others compiled in Table 1). The idea is to select the point on the received signal that corresponds to the arrival of the wave. Although other points have been adopted by some, only the *"Start-to-Start"* (*SS*), *"Peak-to-Peak"* (*PP*) and *"Negative Peak"* (*NP*) methods are shown in Figure 2 as they are by far the most commonly adopted. It is worth noting that, depending on the author, the *NP* travel time can be computed from either the *"Start"* and *"Peak"* points.

Another existing time domain method is *"Cross-Correlation"*. Despite being extremely efficient at detecting the phase delay between two nearly identical signals, it can be difficult to use for bender element testing. Specifically, when

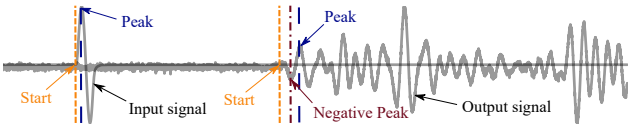

Figure 2: Time domain interpretation of a shear wave signal.

using a single sine period as input electrical signal, the emitting bender element actually oscillates for several periods (Greening et al., 2007). Combined with often inevitable reflections off the sides of the specimen, this makes the emitted and received signals very different, limiting the efficiency of the method.

1.3. Frequency domain methods

The most widespread frequency domain methods are the *"Phase Sensitive Detection"* (*PSD*) methods (Viggiani and Atkinson, 1995; Blewett et al., 1999; Greening and Nash, 2004 among several others). These include the *"Phase Cross Spectrum Method"* and the *"Pi-Point method"*. For both, the general idea is to express phase as a function of frequency and thereby deduce the group velocity v_{gr} of the wave. It is also possible to obtain the phase velocity v_{ph}. Considering a non-dispersive medium, these two velocities are supposed to be identical:

$$v_{ph} = \frac{\omega}{k} = L_{tt}\frac{2\pi f}{\phi}, \tag{1}$$

$$v_{gr} = 2\pi L_{tt}\frac{\mathrm{d}\phi}{\mathrm{d}f} \tag{2}$$

where ω is the angular frequency, k is the wavenumber, L_{tt} is the propagation length, f is the frequency and ϕ is the phase difference between two signals.

Alternatively, a few authors have used wavelet transforms (*WT*) in order to investigate the frequency content of bender element signals and, in some cases, estimate the arrival time. This alternative to the traditional Fourier Transform is particularly efficient at showing the time evolution of the frequency content of a signal. Explanations can be found in Arroyo (2007) and Chen et al. (2020).

1.4. Literature review

Table 1 attempts to compile a significant sample of the research that has been done on bender element testing. Although by no means complete, it shows which interpretation methods have been used or analysed in each paper (separated in *"Time"* and *"Frequency"* methods). It also indicates the type of wave and soil studied, the input signal used and the overall reception of the article as of February 2023. This has been achieved using tallies provided by Scite (Nicholson et al., 2021) and the total number of citations shown on Web of Science (*"WoS"* in the table).

1.5. Arrival picking in geophysics

1.5.1. The STA/LTA ratio

Originally presented by Allen (1978), the STA/LTA algorithm compares the "Short Term Average" (*STA*) with the "Long Term Average" (*LTA*) in order to detect the onset of an earthquake. The two corresponding quantities X_{ST} and X_{LT} can be calculated as:

$$X_{ST} = \frac{1}{N_s}\sum_{n=1}^{N_s} x_n, \tag{3}$$

$$X_{LT} = \frac{1}{N_l}\sum_{n=1}^{N_l} x_n \tag{4}$$

where N_s and N_l are respectively the number of values over which the short or long term averages are calculated. The term x_n is the value of a characteristic function x at the rank n of a signal. According to Vaezi and van der Baan (2015), common parameters are energy, absolute value of the signal and envelope function. For application to bender element interpretation, the square of the signal amplitude was chosen. The long term average is calculated over the entire signal, whereas the *STA* is averaged over a period of time corresponding to the inverse of the peak frequency observed using a Fourier Transform of the signal.

1.5.2. The AIC Method

The "Akaike Information Criterion" is a statistical tool introduced in the 1974 paper by Hirotugu Akaike *"A new look at the statistical model identification"* (Akaike, 1974, later republished in Akaike, 1998). Originally, it was designed for assessing the quality of a model. This is achieved by balancing the natural logarithm of the maximum likelihood $\mathcal{L}_{max}$ of the

	Wave		Specimen			Time						Frequency			Input				Scite Review			WoS
Source	**Vp**	**Vs**	**Sand**	**Clay**	**Other**	**S-S**	**P-P**	**NP**	**CC**	**AIC**	**Other**	**PSD**	**Wavelets**	**Other**	**Sine**	**Square**	**Burst**	**Sweep**	**Supporting**	**Neutral**	**Contrasting**	**Total**
Lawrence et Frederick (1965)		x	x	x							x					x			NA	NA	NA	NA
Shirley et Hampton (1978)		x		x							x					x			0	88	0	268
Dyvik et Madshus (1985)		x		x							x					x			NA	NA	NA	NA
Souto et al. (1994)		x	x		x														1	13	0	25
Viggiani et Atkinson (1995)		x		x		x	x	x	+			+			+	-			4	183	0	361
Brignoli et al. (1996)	x	x	x	x		x									x				NA	NA	NA	271
Jovicic et al. (1996)		x		x		x	x				x				+	-	x		2	106	1	267
Arulnathan et al. (1998)		x	x				x		+		x				x				NA	NA	NA	163
Blewett et al. (1999)		x	x									+			+	-			0	9	0	31
Blewett et al. (2000)		x	x			-	-	-							+	-			0	6	0	53
Arroyo (2001)		x		x		x	x	x	x			x			x	x	x		NA	NA	NA	NA
Kawaguchi et al. (2001)		x		x		+	-	-								x			0	24	0	72
Lings et Greening (2001)	x	x	x												x				0	29	0	95
Arroyo et al. (2003)		x		x											x		x		0	29	0	105
Greening et Nash (2004)		x		x		-	-	-	-			+			x			+	NA	NA	NA	78
Lee et Santamarina (2005)		x	x						+					+	x	x			3	209	0	463
Leong et al. (2005)		x	x	x	x	+	-		-						+	-			NA	NA	NA	128
Rio (2006)		x			x										-	-	+	+	NA	NA	NA	NA
Valle-Molina (2006)	x	x	x			x									x				NA	NA	NA	NA
Nash et al. (2007)		x		x		x						x			x			x	NA	NA	NA	NA
Camacho-Tauta et al. (2008)		x	x	x							+				x				NA	NA	NA	1
Vilhar et Jovicic (2009)		x	x			+			-			-			x				NA	NA	NA	5
Viana de Fonseca et al. (2009)		x	x		x	+						+			+			+	NA	NA	NA	8
Leong et al. (2009)	x	x	x		x	x									x				2	46	0	85
Yamashita et al. (2009)		x	x			+	-		-			-			x	x	x		5	90	0	147
Arroyo et al. (2010)				x	x	x									x				1	5	0	17
Whalley et al. (2011)		x		x			x								x				0	17	0	14
Bonal et al. (2012)		x		x		x	x		x				+		x				1	5	0	20
Alvarado et Coop (2012)		x	x	x		x						x			x				3	25	0	49
O'Donovan et al. (2012)		x			x	x	x		x		+				x				0	16	0	31
Valle-Molina et Stokoe (2012)	x	x	x			x												x	0	4	0	27
Gu et al. (2013)	x	x	x			x									x				2	23	0	94
Ferreira et al. (2013)		x	x			x									x				0	8	0	NA
Zhang et Wang (2014)	x		x							x					x				0	0	0	0
Cai et al. (2015)		x	x			x	+	x	x						x				1	11	0	44
Camacho-Tauta et al. (2015)		x													x			x	1	18	0	27
O'Donovan et al. (2015)		x			x	x	x		x			-			x		x		1	18	0	44
Hasan et Wheeler (2015)	x	x		x			+		-			-			x				NA	NA	NA	NA
Finas et al. (2016)		x		x		x				+									0	2	0	9
Wang et al. (2017)	x	x			x	x	x		x		+	x			x				2	12	0	17
Bialowas et al. (2018)					x					x									0	1	0	4
Kumar et Shinde (2019)		x	x		x	x	x		x					+	x				0	0	0	2
Chen et al. (2020)		x		x		x	x		x				+		x				0	3	0	7

Table 1: Literature review of bender element interpretation methods. While inevitably incomplete, this table attempts to give an overview of previous works concerning both the measurement of compression (v_p) and shear waves (v_s). A neutral grey "x" indicates that the concerned wavetype, specimen, interpretation method or input signal was used in the paper, whereas a green "+" or a red "-" respectively show supporting or contrasting views concerning the method. The interpretation methods are designated by the following acronyms: S-S for *Start-to-Start*, P-P for *Peak-to-Peak*, NP for *Negative Peak*, CC for *Cross Correlation*, AIC for *Akaike Information Criterion* and PSD for *Phase Sensitive Detection*.

model with the number m of independently adjusted parameters in the model, an optimal model can be found where C_{ai} is minimised (Akaike, 1974):

$$C_{ai} = 2m - 2\ln(\mathcal{L}_{max}). \quad (5)$$

As a reminder, the likelihood function $\mathcal{L}$ can be seen as the probability density of observing an event given a set of fitting parameters (Myung, 2003). Considering a seismogram can be separated into two stationary time series modelled each by an auto-recursive process, Sleeman and van Eck (1999) use this criterion to determine an optimal separation point corresponding to the arrival of an earthquake. This optimal separation point is found when the likelihood function $\mathcal{L}$ is maximised which, according to the authors, corresponds to the following expression of the log-likelihood function:

$$\ln(\mathcal{L}) = -\frac{1}{2}(k-m)\ln\sigma^2_{1,max} - \frac{1}{2}(N-m-k)\ln\sigma^2_{2,max} + C \quad (6)$$

where k is the position along the signal of length N maximising the likelihood function while $\sigma^2_{1,max}$ and $\sigma^2_{2,max}$ are respectively the variances of the two stationary processes (before and after wave arrival), m is the order of the auto-regressive model used and C is a constant. Avoiding the use of an auto-regressive process, Zhang et al. (2003) calculate these variances directly from the recorded signal and obtain the expression of *AIC* used in this paper:

$$C_{ai}(k) = k\ln\sigma^2(x[1,k]) + (N-k-1)\log\sigma^2(x[k+1,N]) \quad (7)$$

where $C_{ai}(k)$ is the value of the *AIC* function at the position k of the signal and $\sigma^2(x[1,k])$ corresponds to the variance of the signal taken between indices 1 and k. In other words, minimising this function is equivalent to maximising the probability of observing two stationary processes considering an arrival at the position k. For this reason, the arrival of a wave corresponds to the position k where C_{ai} is smallest.

As can be noted in Table 1, three previous papers mention the use of the Akaike Information Criterion for the interpretation of bender element tests. Zhang and Wang (2014) and Bialowas et al. (2018) mention using the *AIC* to interpret bender element signals on Toyoura sand and crushed chalk respectively but do not seem to experimentally demonstrate the validity of the method. Both studies also apply the *AIC* to the entire recorded signal which, in our experience, regularly causes the method to detect false minima instead of the actual arrival point. Common issues include confusing P and S wave arrivals when near field effect is significant or detecting the disappearance of the signal rather than its arrival. By contrast, the study conducted by Finas et al. (2016) on a stiff clay underlines the need to calculated the *AIC* on a selected window of the signal. They do not, however, provide any automated means of selecting this window. Also, Finas et al. (2016) limit their study to shear wave propagation. Therefore, the main objective is to define an automated method capable of *"focusing"* the *AIC* calculation on an appropriate signal segment for both compression and shear waves.

One might legitimately question the validity of decomposing a bender element recording into two stationary processes. While the stationarity of the *"no signal"* part of recordings seems clear, this approximation can be problematic, especially if amplitude of the signal is very variable during the *"with signal"* segment of the recording. Equally, when compression waves are observed in shear wave signals, the hypothesis is all the more troubling as the segment before arrival is not stationary either. This concern underlines the importance of choosing an appropriate segment of the signal upon which to calculate the *AIC*. This segment must limit the presence of near-field effects and cross-talk while ensuring the segments before and after arrival are as stationary as possible. Two separate algorithms for identifying this segment are proposed and discussed in the rest of the paper.

1.6. Focusing the AIC method

The first proposed method for focusing the *AIC* is to take the emission of the signal as the start point and the maximum amplitude as the end point. From here on, this method will be named *"Maximum-AIC"* or *MAIC* for short. Figure 3 illustrates

the different steps in this process.

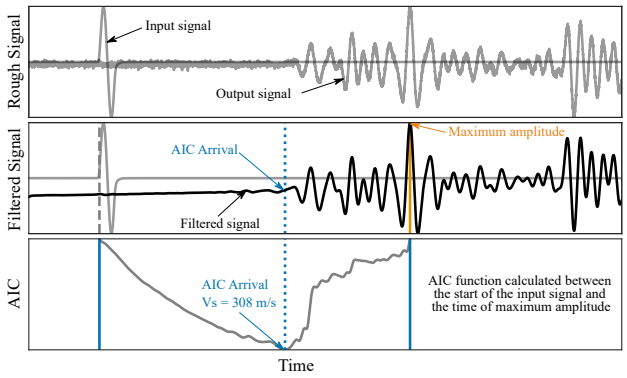

Figure 3: Shear wave arrival detection using the *MAIC* method.

An alternative method, named *"STA-LTA-AIC"* or *SLA* for short, is inspired by the works of Akazawa (2004). The general idea is to use the *STA-LTA* ratio to locate the high amplitude section of the signal. Then, two successive uses of the *AIC* function help distinguish compression waves from shear waves. Initially, the *AIC* is calculated between a start point corresponding to the emission of the input signal and the first point for which the *STA-LTA* ratio indicates the presence of a signal. The aim of this iteration is to separate the recording into a stationary segment containing background noise and a short segment containing a small number of periods. This small number of periods ensures the second segment can just about be approximated as stationary. It also allows the arrival point detected this way to correspond to the earliest possible arrival, even when its amplitude is relatively small. When measuring compression waves, this arrival point should provide a good estimation of velocity.

When measuring shear waves, the arrival point obtained after the first iteration will, if they exist, systematically correspond to compression waves. For this reason, the *AIC* is calculated again, this time on a segment going from just before the previously detected arrival to the end of the high-amplitude segment of the signal as determined using the *STA-LTA* ratio. This second segment must first ensure that, in the absence of compression waves, the second iteration will result in the same arrival point being detected. Then, it must also guarantee that the new segment can be decomposed into two relatively stationary signals, one corresponding to near-field components and the other to the actual signal of interest. For this, trial and error showed that the starting point could be taken one period before the previously detected arrival. This period is estimated as the inverse of the peak frequency of the Fourier transform of the complete signal as shown in Figure 4. Choosing the end point as the end of the high-amplitude segment of the signal makes sure that the amplitude of shear wave signal is not too variable, thereby satisfying the stationarity hypothesis as much as possible.

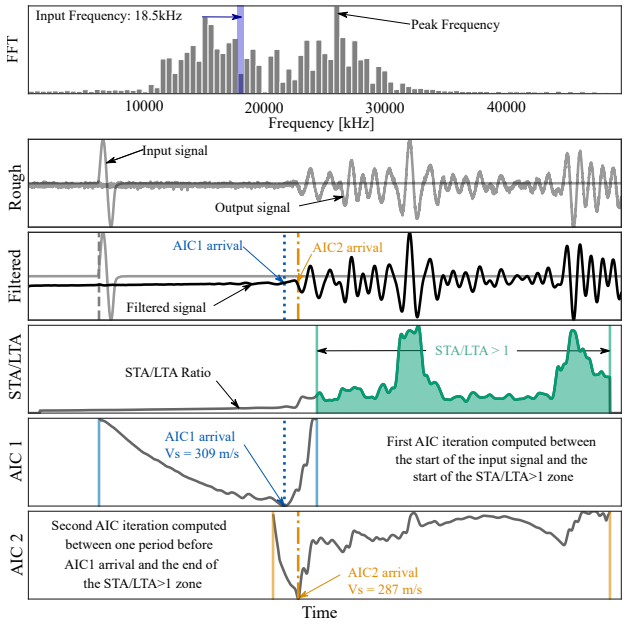

Figure 4: Shear wave arrival detection using the *SLA* method.

2. Testing the algorithms

2.1. Experimental data

Both interpretation methods were tested on a set of over 15,000 signals containing dry, saturated and gassy ($S_r \geq 0.9$) Fontainebleau sand. While this happens to be the database of bender element signals available to us, it is worth noting that the focus of this paper is mainly on the performance of the algorithms, rather than on the mechanical behaviour of the sand. The sand parameters used in this study are compiled in Table 2.

The sands were mostly prepared by air pluviation with density indices I_d of 0.92 and 0.54. Table 3 provides a list of the

Property	Value	Source
D_{50} [mm]	0.223	Andria-Ntoanina (2011)
C_u	1.48	Andria-Ntoanina (2011)
e_{max}	0.866	Andria-Ntoanina (2011)
e_{min}	0.545	Andria-Ntoanina (2011)
ρ_s [kg/m^3]	2650	Andria-Ntoanina (2011)
K_s [GPa]	37	Subramaniyan et al. (2015)

Table 2: Median grain diameter, granulometric uniformity coefficient, maximal and minimal void ratios, solid grain density and grain bulk modulus considered for NE34 Fontainebleau Sand.

different sand specimens prepared. The void ratio is obtained by repeating at least seven times the calibration process and deducing the mean and standard deviation. A confidence interval of 95% was adopted with Student's t-distribution in order to describe the error of the pluviation process. For the single specimen prepared by dry tamping, the uncertainty is deduced from the precision of the instruments used to measure mass and volume.

Specimen	Void ratio	Preparation
Id92-H200-v1	0.56±0.01	Pluviation
Id92-H200-v2	0.56±0.01	Pluviation
Id92-H200-v3	0.57±0.007	Dry tamping
Id92-H200-v4	0.56±0.01	Pluviation
Id92-H200-v5	0.56±0.01	Pluviation
Id92-H100-v1	0.56±0.01	Pluviation
Id92-H100-v2	0.56±0.01	Pluviation
Id54-H200-v1	0.69±0.04	Pluviation
Id54-H200-v2	0.69±0.04	Pluviation
Id54-H200-v3	0.69±0.04	Pluviation
Id54-H200-v4	0.69±0.04	Pluviation
Id54-H200-v5	0.69±0.04	Pluviation
Id54-H200-v6	0.69±0.04	Pluviation
Id54-H200-v7	0.69±0.04	Pluviation
Id54-H200-v8	0.69±0.04	Pluviation

Table 3: List of tested sand specimens. The name of each experiment indicates the density index I_d and the height of the specimen (the diameter is always 100 mm).

2.2. Experimental apparatus

The experiments were executed using a set of bender-extender elements purchased from GDS Intruments. The protruding length of elements was of 3.5±0.5 mm. The *"same polarisation"* element was set into the bottom platen of a triaxial cell while the *"opposite polarisation"* element was set at the top end.

The signal was generated using a TG1010A function generator, while the received signal was observed on an Agilent Technologies InfiniiVision DSO-X-2004A digital oscilloscope and recorded using Labview. The input signal was a single sine period of variable frequency, ranging from 1 to 50 kHz for shear waves and from 1 to 200 kHz for P waves. As is relatively common practice in bender element testing (Shirley and Hampton, 1978; Nakagawa et al., 1997; Blewett et al., 1999; Leong et al., 2005; Rio, 2006; Leong et al., 2009; Camacho-Tauta et al., 2015), a light band-pass filter was also applied to improve signal quality. Two passes of a first order butterworth filter were used to avoid introducing phase shifts into the signal. The passband was centered around the input frequency while its width corresponded to 60 kHz. The amplitude of the passband was chosen to ensure that white noise was significantly reduced while the signal of interest was unaltered.

2.3. Statistical analysis of the MAIC and SLA methods

In order to analyse the efficiency of the *MAIC* and *SLA* algorithms, the results of these two automated interpretations are compared with those obtained using a more *"traditional"* method. As this analysis was performed on a large number of signals, it was unpractical to use more than one manual interpretation method.

Frequency domain methods were avoided as they are very sensitive to the range of used frequencies and have been reported to be less reliable than time domain methods (Yamashita et al., 2009). Despite some positive feedback for both time domain methods (see Table 1), the *"Start-to-Start"* method was preferred to the *"Peak-to-Peak"* method. This was mainly due to two theoretical considerations. Firstly, as the electrical input

frequency is not generally the same as the dominant frequency of the received signal, the resulting velocity could be artificially sensitive to the frequency. Secondly, constructive or destructive interferences in between the different components of the received signal could hide its first *"real"* peak.

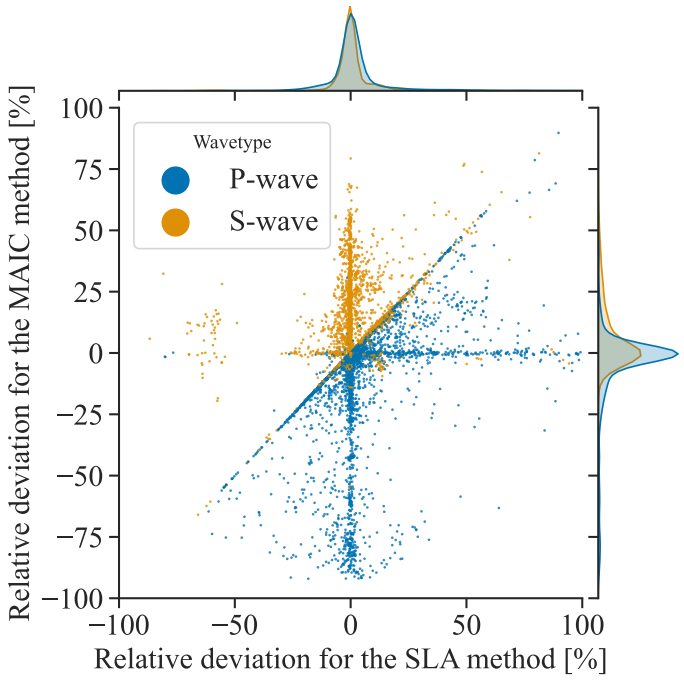

Figure 5: Comparing the relative deviation of the *SLA* and *MAIC* interpretation methods on grade one (and above) signals. The deviation is expressed with respect to a manual estimation using the Start-to-Start method. The observed diagonal lines indicate signals where both algorithms returned similar results differing from the manual interpretation while centered vertical and horizontal lines show that only one of the two algorithms is inconsistent with the manual interpretation.

Figure 5 shows the distributions of relative velocity deviations correponding to the *SLA* and *MAIC* methods as a percentage of the first arrival velocity obtained manually. Each individual dot corresponds to a measurement whereas the lateral density plots show the deviation distribution for each method. Table 4 provides the mean and the standard deviation of the distribution for both *SLA* and *MAIC* algorithms. Throughout this article, relative deviation is expressed in percentages and calculated as:

$$D_X = \frac{v_X - v_{ss}}{v_{ss}} \tag{8}$$

with X corresponding either to *SLA* or *MAIC* according to which deviation is being calculated and v_{ss} is the wave velocity computed using the Start-to-Start manual method (*SS*).

Method	**Grade**	**Type**	**Mean**	**Standard Deviation**
MAIC	1	v_p	-5.9%	19.2%
MAIC	1	v_s	8.3%	24.2%
MAIC	5	v_p	-1.8%	10.2%
MAIC	5	v_s	1.1%	5.8%
SLA	1	v_p	3.0%	17.0%
SLA	1	v_s	0.7%	11.5%
SLA	5	v_p	1.1%	7.6%
SLA	5	v_s	-0.3%	4.1%

Table 4: Relative velocity deviation distribution of the SLA and MAIC methods.

From this representation of relative deviation, we can observe several features. First of all, as illustrated by the lateral density plots, the relative velocity deviation is closer to zero in the horizontal direction than in the vertical direction. This indicates that the *SLA* method is generally in better agreement with manual Start-to-Start interpretation than *MAIC*. On average, *MAIC* has a tendency to overestimate the shear wave velocities and underestimate the compression wave velocities. This is generally due to the presence of both compressive and shear components in many recordings. Possible explanations for these observations could include near-field effects, lateral wave reflections or the behaviour of the emitting bender-extender element. This specific topic is discussed further in the appendix.

The result of the presence of both compression and shear components is that, when looking for shear waves, *MAIC* occasionally picks up on faster compression waves, thereby overestimating velocity. Similarly, when interpreting compression waves, shear components can end up having greater amplitude than the compression wave of interest. If such high amplitude shear components are inside the window over which *AIC* is computed, the global minimum for that window will correspond to the shear waves, resulting in an underestimation of P-wave velocity. By contrast, the *SLA* is generally better suited at dealing with these undesired wave components as it focuses

the *AIC* window away from them.

Figure 5 contains data from all the measurements in our database with no consideration given for the quality of the signal. Any phenomenon complexifying the signal, such as cross-talk, near-field effect or attenuation is just as likely to confuse these algorithms as it is a human being. This goes some way to explaining the significant velocity differences shown in Figure 5.

In order to account for the varying quality of the signals, a grade was given to them ranging from 0 to 5. A grade of "0" indicates the signal is unusable, while a grade of "5" is given when the arrival point is absolutely unmistakable to human eyes. Figure 6 presents a selection of shear wave signals corresponding to grades 0 through 5. As an example, the first signal gets the grade 0 as the signal baseline is gradually drifting from positive to negative values. This type of defect in the recorded signals causes both algorithms to fail regularly. While the grade attributed here is debatable as the signal can be interpreted manually, the choice seems reasonable as this behaviour should not be observed in any well recorded signal. Alternatively the grades 1 to 3 are given according to how strongly the undesired compression or shear components are contaminating the recording. Keeping only grade 5 signals, Figure 7 shows that the performance of the both algorithms is considerably improved.

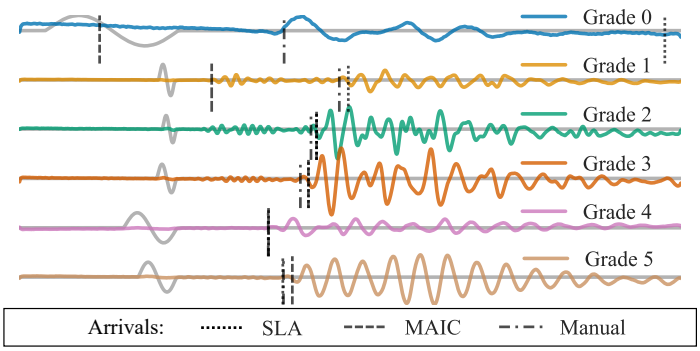

Figure 6: Illustration of signal grade attribution. Increasing grades show improving signal quality. Grades of zero indicate that the signal is in some way corrupted (in this case the signal baseline is drifting) while grades of five are given only to good quality signals where wave arrival is absolutely unmistakable to the naked eye.

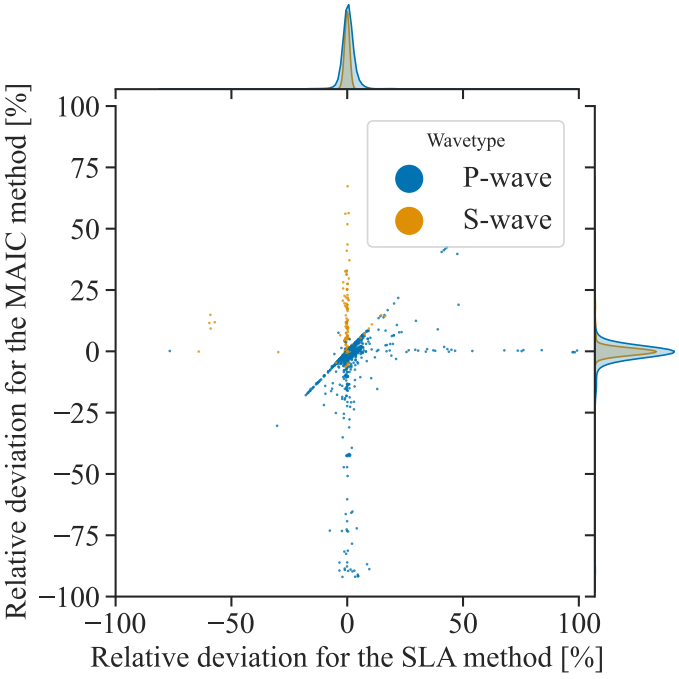

Figure 7: Comparing the relative deviation of the *SLA* and *MAIC* interpretation methods on grade five signals.

As could be expected, both algorithms are in much better agreement with manual interpretation when very clear signals are used. It is however important to note the presence of outliers, even for high quality signals. Assuming wave velocity is constant within a given frequency range, this issue can be addressed by taking the median result out of a group of measurements at different frequencies. This process has the added benefit of providing a standard deviation and therefore an estimation of the precision of the interpretation process.

On both Figures 5 and 7, a diagonal line going from bottom left to top right is visible. This corresponds to the points where both automated interpretations agree on a velocity that is different from that obtained manually. This can occur when the *AIC* algorithm is picking up on a specific feature of the signal that is not what interests the person doing the manual interpretation. Occasionally, it can also be a sign that the manual interpretation was incorrect. Meanwhile, the centered vertical and horizontal lines indicate signals where only one of the two algorithms has failed. In order to better identify the strengths and weaknesses of the algorithms, the performance of each algorithm are anal-

ysed in greater detail in the two following sections.

2.4. Testing the SLA algorithm

Concentrating on the performance of the *SLA* algorithm, Figure 8 shows the distribution of relative deviation considering three different saturation states and five signal grades. The boxplots indicate the mean relative deviation, as well as the 25th, 50th and 75th percentiles (noted respectively P_{25}, P_{50} and P_{75}).

From this figure, one can observe that, for signals with a grade of three or over, the median value is satisfyingly close to zero. Bearing in mind that uncertainty in wave velocity measurements using bender elements is reported to reach up to 50% (Arroyo, 2001), the spread also seams reasonable. Unfortunately, the method does still occasionally fail with good quality signals. Although this is to be expected with any interpretation algorithm, it is a clear indication that there is still room for improvement.

Concerning the interpretation of bender element tests in gassy sands, the *SLA* method has a tendency to seriously overestimate the P-wave velocity for low-grade signals. As shown by Astuto et al. (2022) and Flood-Page et al. (2023), compression waves generated by bender elements in gassy soils tend to contain multiple phases travelling at different velocities. These signals are very complex to interpret as several arrival points could justifiably be chosen. Consequently, *SLA* might disagree with manual interpretation without either method necessarily being wrong. Due to the complexity of such signals, they are often given low grades, explaining why the relative velocity deviation is particularly significant for grades below four. As the *SLA* algorithm is deliberately designed to pick up on the earliest possible arrival, the difference is systematically positive. For instance, with signals where one might manually choose a slower component with higher amplitude, the algorithm will instead detect the faster component with much lower amplitude. By contrast, the interpretation of S-wave signals in gassy sands is much simpler, which explains why algorithm and manual interpretation tend to agree more readily. In the case of measurements in dry and saturated soils, the algorithm generally performs well for both shear and compression waves with one main exception. On some dry specimens, a faster compression wave was observed at higher frequencies. The effect is particularly visible on P-wave measurements as the *SLA* algorithm systematically picks the fastest arrival, but can also have an impact on shear wave interpretation. As these signals were given low grades, this overestimation of v_p and v_s is only really visible for grades one and two.

2.5. Testing the MAIC algorithm

Figure 9 shows the relative deviation distribution for the *MAIC* method. At a first glance, one can confirm that the reliability of this method is considerably less than the *SLA* method. This is visible as the median deviation is more variable than that of *SLA* and the distribution is far more spread out.

Despite being less reliable, this method can still be of some use. Where the *SLA* method picks the very first arrival for compression waves and the last possible arrival for shear waves, *MAIC* is far more sensitive to the amplitude of the signal. This tendency is particularly visible when comparing the *SLA* and *MAIC* deviation distributions. Where the first makes a habit of overestimating v_p, the latter often underestimates it. This feature can be of interest for a few applications such as the interpretation of P-wave signals on dry soils. As shown in Figure 10, a faster compression component can sometimes be observed at higher frequencies. This phenomenon was exclusively observed when using a confinement fluid to generate effective stress (as opposed to a vacuum pump). Therefore, the presence of this faster compression wave could potentially be explained by the infiltration of water into the specimen if it were not perfectly watertight. Alternatively, compression waves could also be propagating through the water in the confinement cell. This hypothesis seems more likely as these faster compression waves were also observed on specimens where the absence of moisture was verified at the end of the experiment.

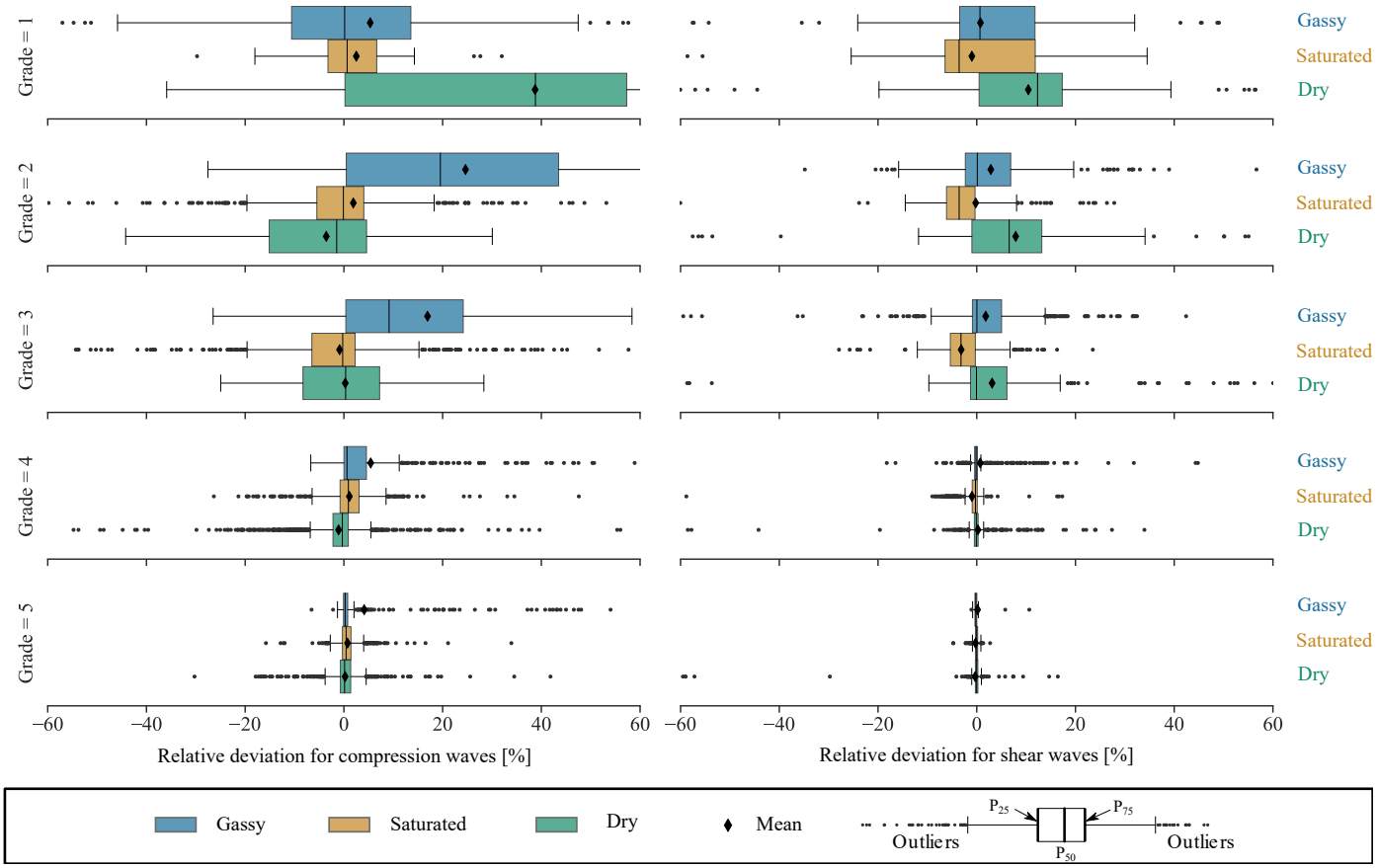

Figure 8: Velocity computed by the *SLA* algorithm compared with manual interpretation. Generally, this method seems better at estimating velocities for shear waves than for compression waves. The tendency to overestimate velocity can be understood as this method is designed to detect the earliest possible arrival, regardless of the overall amplitude of the signal. The length of the *"whiskers"* of the boxplots is set at 1.5 times the interquartile range. This fairly standard value for boxplots defines which points are considered as outliers.

3. Using the algorithms

3.1. General recommendations

Using the *AIC*-based algorithms for interpreting bender element tests provides an alternative to traditional time methods such as *"Start-to-Start"* or *"Peak-to-Peak"*. Its main advantage is repeatability. Anyone using these algorithms will obtain exactly the same velocity out of the same signal. However, as they are currently implemented, the algorithms are not capable of estimating the quality of the signal beyond a simple estimation of the signal-to-noise ratio. A few procedures can be combined in order to ensure the quality of the results:

- Eliminating all signals where the algorithm has visibly failed. This can be done by setting bounds for realistic values of wave velocities.
- Taking a very wide range of signals at slightly different frequencies. Besides giving valuable information on dispersion, this significantly improves the reliability of the interpretation. Using the median value of this set of measurements, rather than the mean, is highly recommended.
- The *SLA* algorithm provides two potential arrival points. According to the type of soil being tested, it is possible to choose one or the other. It can also be helpful to compare the results of *SLA* and *MAIC*.
- Filtering out all signals with low Signal-to-Noise ratios can be an alternative to manually eliminating poor or bugged signals. This can help make the interpretation process fully automated.

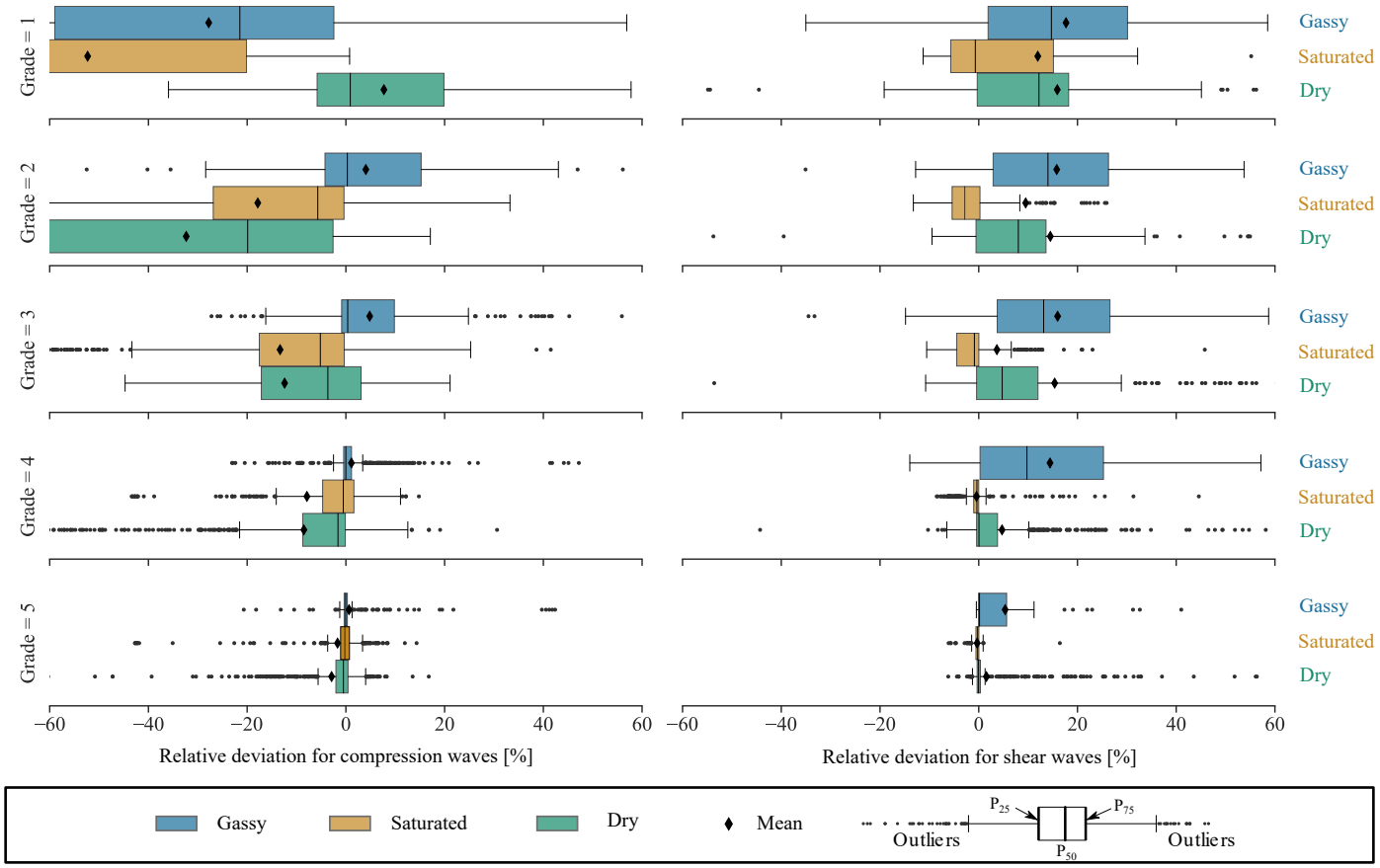

Figure 9: Velocity computed by the *MAIC* algorithm compared with manual interpretation. This method is, on average, less reliable than *SLA*. However, *MAIC* noticeably outperforms *SLA* for grade one compression waves on dry specimens.

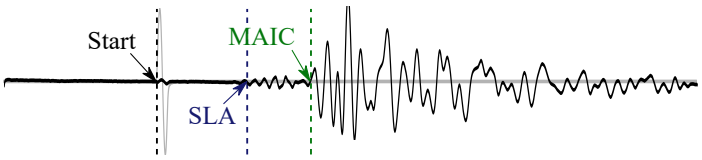

Figure 10: Effect of a faster compression wave on *SLA* and *MAIC* interpretation. This faster wave component is only observed when the specimen is surrounded by a confinement fluid, showing that it is not representative of the dry specimen behaviour.

3.2. Small strain moduli for Fontainebleau sand

In order to illustrate the use of the *AIC* algorithms for bender element testing, they are used here to determine the shear and oedometric small-strain moduli G_0 and M_0 for Fontainebleau NE34 sand:

$$G_0 = \rho v_s^2, \tag{9}$$

$$M_0 = \rho v_p^2. \tag{10}$$

where the density ρ corresponds either to the dry or saturated density according to the state of the soil, while the dry density ρ_d is deduced from the void ratio in Table 3 and the density of the sand grains given in Table 2.

Figure 11 shows the S and P wave moduli obtained for dry Fontainebleau sand using bender-extender elements. The results were calculated using what we shall call a *"mixed" AIC* interpretation. The shear waves are exploited using the *SLA* algorithm while the compression wave velocities come from the *MAIC* algorithm. This combination is practical for testing dry specimens as *SLA* is far more robust for shear waves, while *MAIC* has the advantage of being relatively insensitive to any unwanted faster compression waves (example shown in Figure 10). It can be compared with Figure 12 providing the results of the manual interpretation on the same set of data.

For both graphs, each point represents one specimen at a spe-

cific level of effective pressure. At each of these pressure levels, a range of frequencies are tested and all signals are kept, regardless of the attributed grade. The position of the marker represents the median value P_{50} of this group of signals, while the confidence interval, if shown, is calculated using a normal distribution for a confidence level of 95%.

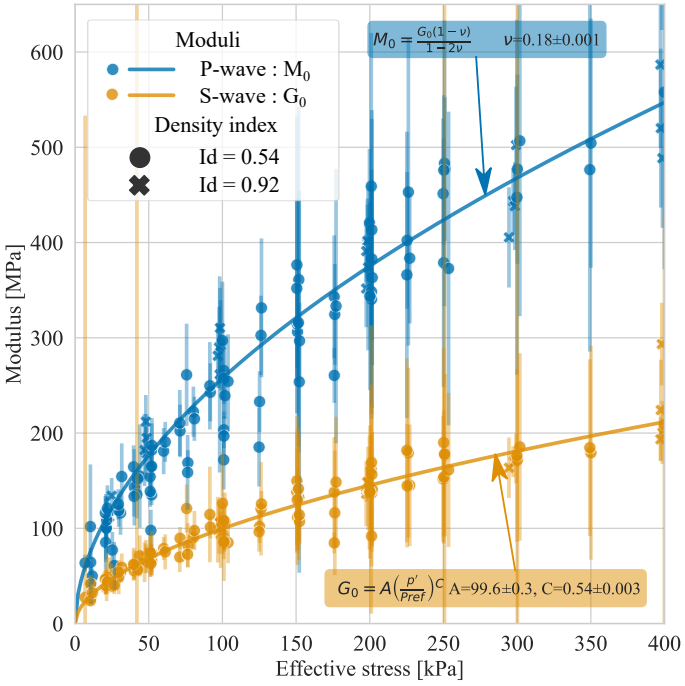

Figure 11: Small-strain moduli found for dry Fontainebleau sand: *"mixed"* interpretation. Each dot correponds to the median value of a range of measurements at different frequencies while the vertical error bars are deduced from the corresponding standard deviation, considering a normal distribution and a 95% confidence level.

Although an effect of void ratio on both shear and oedometric modulus is expected (Goudarzy et al., 2018; Menq, 2003; Tatsuoka et al., 1979; Wichtmann and Triantafyllidis, 2010), no clear impact of void ratio was noted using either the *manual* or *mixed* methods. A likely explanation is that the uncertainty resulting from the experimental setup is greater than the effect of void ratio. For this reason, a simple fitting curve was used for G_0:

$$G_0 = A\left(\frac{p'}{P_{ref}}\right)^C. \tag{11}$$

The small strain P-wave modulus M_0 is considered to be a function of the Poisson ratio ν and the small strain shear modulus

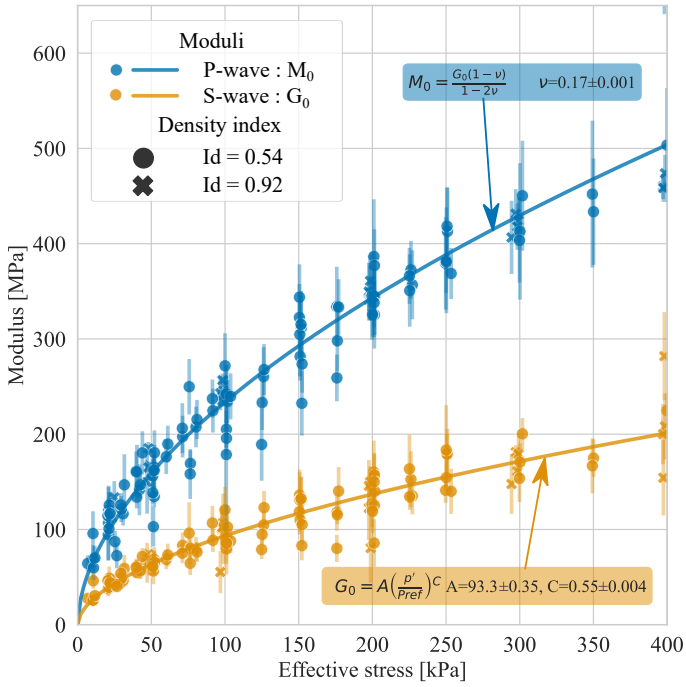

Figure 12: Small-strain moduli found for dry Fontainebleau sand: *"Manual"* interpretation.

G_0. Therefore, fitting the P-wave data provides an estimate of the Poisson ratio:

$$M_0 = \frac{1-\nu}{1-2\nu}G_0. \tag{12}$$

The fitting parameters given in Table 5 were obtained using the Levenberg-Marquardt algorithm as implemented in the *"curve_fit"* function provided by SciPy (Virtanen et al., 2020). The confidence interval on each parameter is estimated from the covariance matrix of the fitting process with a confidence level of 95% and a normal distribution.

As the difference between compression and shear wave velocity is much greater in saturated conditions than with dry sands, estimation of shear modulus was generally far more accurate in saturated sands. For this reason, Figures 13 and 14 provide a more precise estimation of shear modulus, capable of accounting for the effect of void ratio. In these conditions, the small strain behaviour is fitted using Equation (13):

$$G_0 = A\frac{(B-e)^2}{1+e}\left(\frac{p'}{P_{ref}}\right)^C. \tag{13}$$

Small strain shear moduli obtained on dry and saturated Fontainebleau sand are compared in Figure 15 with results pre-

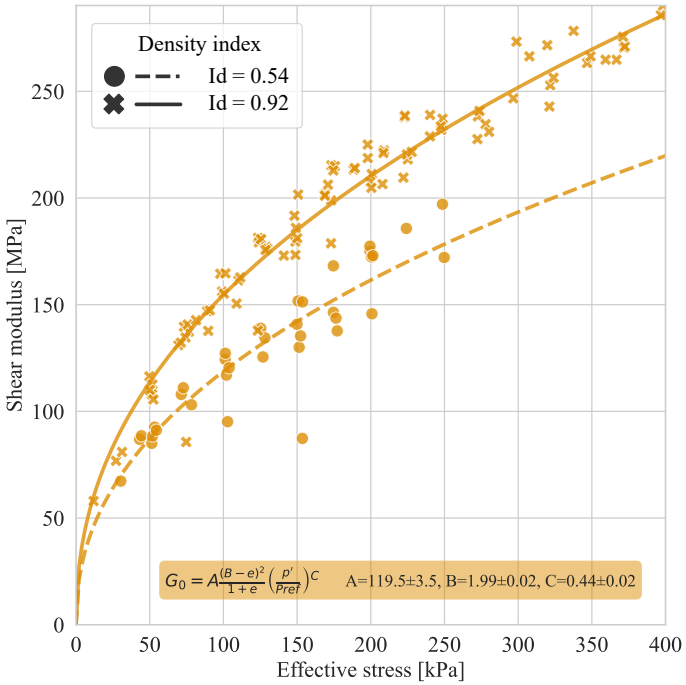

Figure 13: Small-strain shear moduli found for saturated Fontainebleau sand: *"SLA"* interpretation.

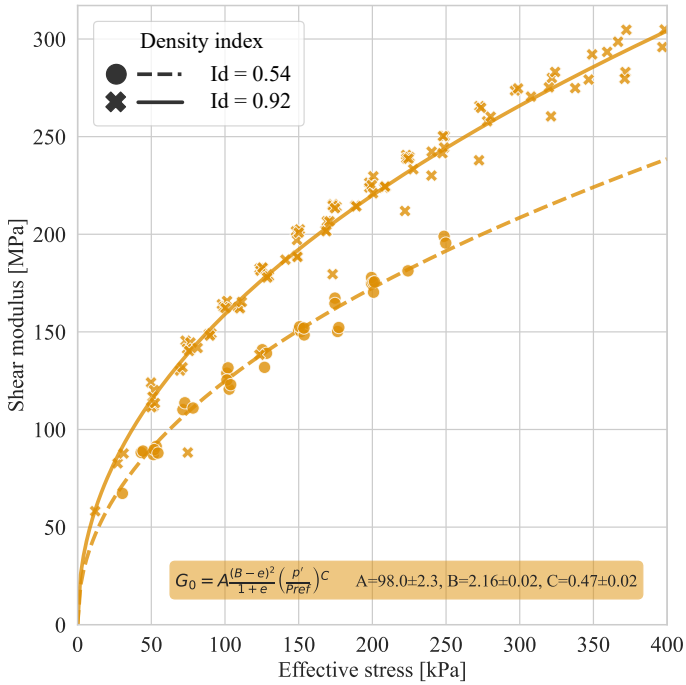

Figure 14: Small-strain shear moduli found for saturated Fontainebleau sand: *"Manual"* interpretation.

viously obtained by Delfosse-Ribay et al. (2004) using a resonant column apparatus. While bender element measurements performed on saturated sand seem to give larger estimates of shear modulus, they remain within the 100% error margin suggested by Arroyo (2001) when estimating shear modulus from bender element tests. It remains unclear whether the difference between dry and saturated measurements is due to hypothetical differences in specimen preparation or to the inherent uncertainty of bender element testing. Nevertheless, it is important to note that the deviation observed between *SLA* and manual interpretation is much smaller than that between different sets of measurements.

Conclusions

The aim of this paper was to present and test different implementations of the *"Akaike Information Criterion"* for the interpretations of bender element tests. Previous attempts have shown that one of the main challenges when using this approach is the need to define a window in which to calculate the *AIC*. Therefore, the core work presented here consists of two possible algorithms for automatically defining this window. Overall, this approach to interpreting bender element tests has two main advantages: repeatability and efficiency. Our experience shows it is most helpful when interpreting complex signals for which several arrival points could legitimately be chosen manually, or for very large datasets where manual interpretation is prohibitive.

A comprehensive database of bender element signals was used in order to illustrate the potential of the *AIC* for the interpretation of bender element tests. Containing signals obtained on dry, saturated and gassy Fontainebleau sand, this database helped examine two possible implementations of the *AIC* function: the *SLA* and *MAIC* algorithms. The results of these automated interpretation methods were compared with those obtained manually using the *"Start-to-Start"* time domain method.

The main conclusions of the statistical analysis of the deviation between manual and automated interpretation showed that the *SLA* algorithm was considerably more robust than *MAIC*. However, this general observation hides significant variations in

Data	Interpretation	Grade	A [MPa]	B [-]	C [-]	*nu* [-]
Delfosse-Ribay et al. (2004)	N/A	N/A	68.2	2.17	0.47	N/A
Dry	Manual	1	93.3±0.3	N/A	0.55±0.004	0.17±0.001
Dry	Mixed	1	99.6±0.3	N/A	0.54±0.003	0.18±0.001
Saturated	Manual	1	98±3	2.16±0.03	0.47±0.02	N/A
Saturated	SLA	1	119±4	1.99±0.02	0.44±0.02	N/A

Table 5: Fitting parameters for small strain moduli on Fontainebleau sand. The data from Delfosse-Ribay et al. (2004) corresponds to resonant column tests.

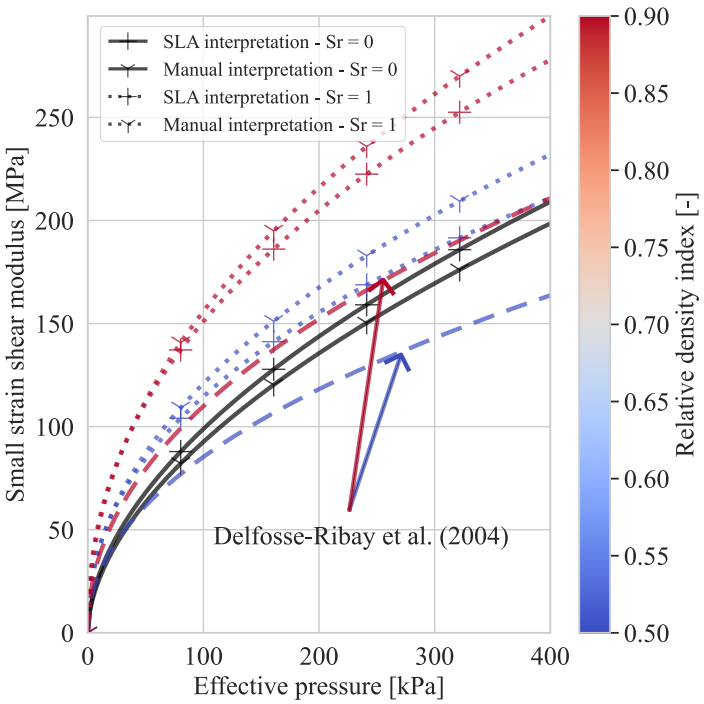

Figure 15: Small strain moduli obtained from dry and saturated Fontainebleau sand compared with results previously obtained by obtained by Delfosse-Ribay et al. (2004) using a resonant column. Overall, the deviation observed between manual and *SLA* interpretation is considerably less than that observed between different observations of the small strain shear modulus. The fitting parameters used to plot these curves are given in Table 5.

performance induced by the type of specimen and wave being tested. For instance, *SLA* is designed to detect the earliest possible P-wave arrival with little regard for its amplitude, while *MAIC* is far more sensitive to the point of maximum amplitude. Consequently, the former is most suited for detecting P-waves in saturated and gassy soils whereas the latter is better at measuring v_p in dry specimens. Similarly, the *SLA* algorithm expects to find both compression and shear waves in every signal. This explains why it is far more efficient when both compression and shear components are visible on the same recording.

All in all, this paper has highlighted the potential of the *AIC* function for building automated time-domain interpretation algorithms. However, it is worth noting that those presented here are but two of many possible implementations of the function. Equally important, they have currently only been tested on Fontainebleau sand and could prove less efficient on other types of soil. Therefore, considerable improvements upon the proposed algorithms could definitely still be proposed.

Acknowledgements

We would like to thank Marine Lemaire, Emmanuel Delaure and Baptiste Chabot from the Navier technical team for the help they provided during these experiments. We are also grateful to Matthew Coop for his valuable advice concerning the use of bender elements and to Maxime Pierre for suggesting the Akaike Information Criterion to us. Finally, we would like to acknowledge the constructive feedback from Alain Pecker and Pierre Delage.

Declaration of Competing Interest

The authors declare that they have no known competing financial interests or personal relationships that could have appeared to influence the work reported in this paper.

Data availability

While the exact algorithms have not been openly published in accordance with the wishes of Egis, the company funding this

piece of work, they can be shared on demand for exclusively academic purposes. The full dataset presented in this paper will be available online from the first of January 2024. The details of the repository are:

- Repository: *https://entrepot.recherche.data.gouv.fr*
- Licence: *etalab-2.0*
- DOI: *https://doi.org/10.57745/XLPRVO*

Appendices

Relative velocity analysis

Tables 6 and 7 provide the numerical values for statistical parameters presented respectively in Figures 8 for the *SLA* algorithm and 9 for the *MAIC* algorithm.

As an alternative to studying relative deviation in Figures 8 and 9, a study of relative velocity was also performed in case any bias might be hidden because of the tool chosen to present the data. Figures 16 and 17 show the ratio between the algorithm-computed velocity and the manually interpreted velocity. The general trends observed using relative velocity being practically identical to those obtained using relative deviation, both figures and the corresponding data tables are only mentionned here as an appendix.

Near-field effects and piezo-electric element behaviour

In Section 2.3, a question is raised concerning the observation of both compression and shear components in a number of recorded signals. Three possible explanations were suggested: near-field effect, lateral wave reflections and the behaviour of the emitting bender-extender element. To test these hypotheses, Figures 18 and 19 respectively show the effect of estimated wavelength on relative deviation for the *MAIC* and *SLA* algorithms.

Theoretically, these hypotheses can be tested by looking at the effect of frequency on the relative deviation between manual and automated interpretation. Near-field effects should only be observed within a couple of wavelengths of the source (Barrière et al., 2012; Sanchez-Salinero et al., 1986). For specimens with a length of 0.2 m, this implies that waves can start to satisty this criterion for wavelengths below 0.1 mm. Meanwhile, considering a specimen radius of 0.05 m, one could assume that waves with wavelengths below 0.01 m should not be too heavily affected by lateral wave reflections. Looking at compression waves on the left side of Figures 18 and 19, there does not seem to be any clear trend showing that relative deviation is improved for wavelengths below 0.1 m, suggesting near-field effects are not the main issue. One could argue that an improvement is noted below 0.01 m, implying that lateral boundary conditions are a more likely source of error. However, this trend is at best faint and one must remember that, on average, precision of both manual and automated picking procedures will inevitably be better at low frequencies due to the smaller interval between signal peaks.

As for shear waves, there does generally seem to be an increase in relative deviation as wavelengths near 0.1 m for both *MAIC* and *SLA*, possibly suggesting near-field effect is a possible culprit. Nevertheless, with regards to *MAIC* interpretation in Figure 18, there seem to be two main concentrations of off-center dots. This could possibly point to there being two separate causes for the presence of compression wave components on shear wave recordings. One could notably imagine that, at higher frequencies, the bender element does not behave as a simple bending beam, thereby introducing compression waves into the specimen. Meanwhile, at lower frequencies, the bender element behaves better but, this time, near-field effects could be responsible. A consequence of this hypothesis would be that *SLA* is better at interpreting shear waves at higher frequencies, while both are similarly affected by near-field effects.

References

Achenbach, J.D., 1975. Wave Propagation in Elastic Solids. Number 16 in North Holland Series in Applied Mathematics and Mechanics. 7. impr ed., Elsevier, Amsterdam.

Akaike, H., 1974. A new look at the statistical model identification. IEEE Transactions on Automatic Control 19, 716–723. doi:10.1109/TAC.1974.1100705.

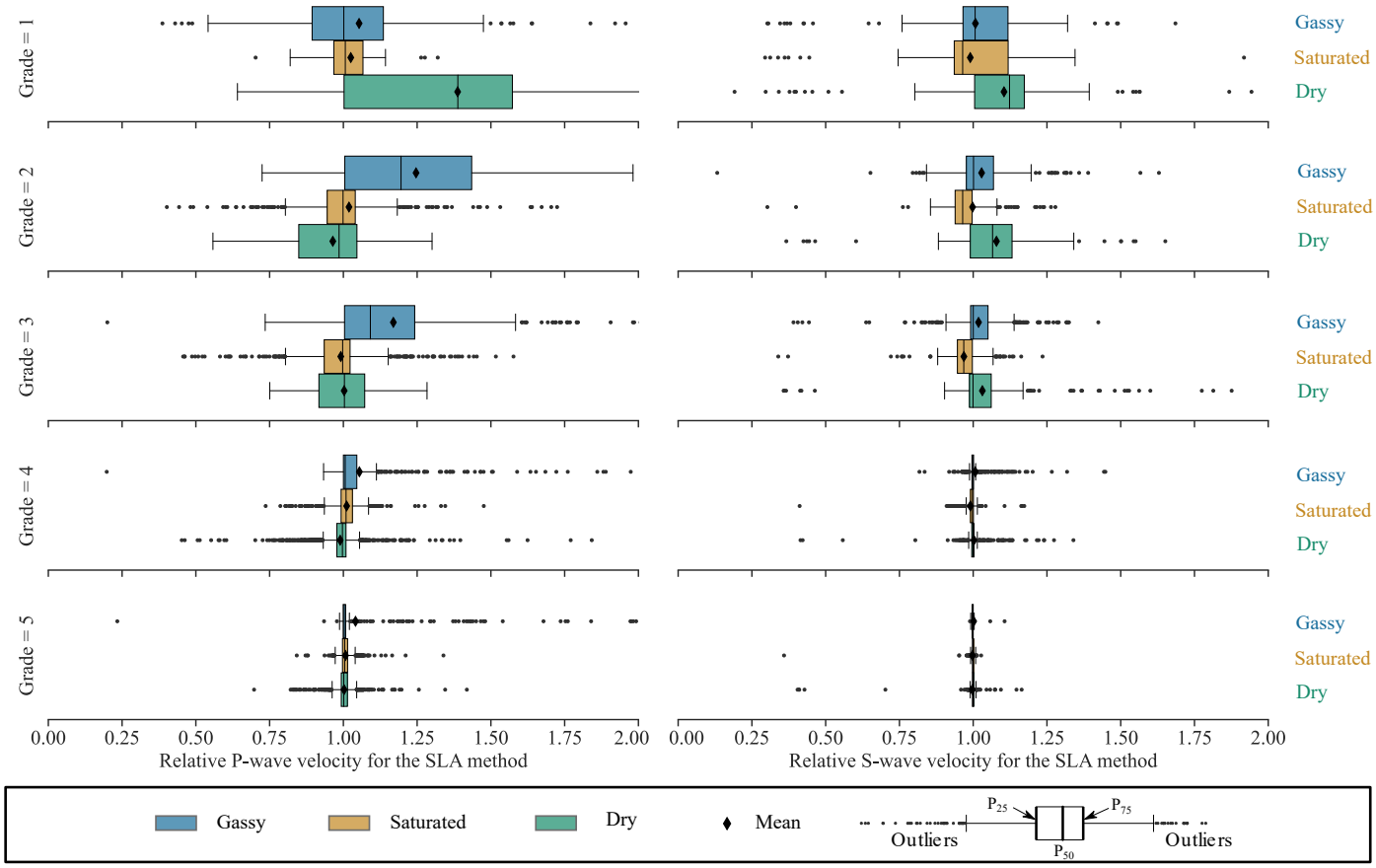

Figure 16: Ratio between the velocity determined using the *SLA* algorithm and the manual *Start-to-Start* method. Values greater than one indicate that *SLA* is overestimating the velocity and correspond to positive values of relative deviation. As in previous boxplots, the length of the *"whiskers"* is set at 1.5 times the interquartile range.

Akaike, H., 1998. Selected Papers of Hirotugu Akaike. Springer Series in Statistics, Springer New York, New York, NY. doi:10.1007/978-1-4612-1694-0.

Akazawa, T., 2004. A technique for automatic detection of onset time of P- and S-phases in strong motion records, in: Proc. of the 13th World Conf. on Earthquake Engineering, Vancouver, Canada.

Allen, R.V., 1978. Automatic earthquake recognition and timing from single traces. Bulletin of the Seismological Society of America 68, 1521–1532. doi:10.1785/BSSA0680051521.

Alvarado, G., Coop, M., 2012. On the performance of bender elements in triaxial tests. Géotechnique 62, 1–17. doi:10.1680/geot.7.00086.

Andria-Ntoanina, I., 2011. Caractérisation Dynamique de Sables de Référence En Laboratoire - Application à La Réponse Sismique de Massifs Sableux En Centrifugeuse. Ph.D. thesis. Université Paris-Est. Champs sur Marne, France.

Arroyo, M., 2001. Pulse Tests in Soil Samples. Ph.D. thesis. University of Bristol. Bristol, United Kingdom.

Arroyo, M., 2007. Wavelet analysis of pulse tests in soil samples. Rivista Italiana di Geotecnica (2) .

Arroyo, M., Greening, P.D., Muir Wood, D., 2003a. An estimate of uncertainty in current laboratory pulse test practice. Rivista Italiana di Geotecnica 37, 17–35.

Arroyo, M., Muir Wood, D., Greening, P.D., 2003b. Source near-field effects and pulse tests in soil samples. Géotechnique 53, 337–345.

Arroyo, M., Muir Wood, D., Greening, P.D., Medina, L., Rio, J., 2006. Effects of sample size on bender-based axial G0 measurements. Géotechnique 56, 39–52. doi:10.1680/geot.2006.56.1.39.

Arroyo, M., Pineda, J.A., Romero, E., 2010. Shear Wave Measurements Using Bender Elements in Argillaceous Rocks. Geotechnical Testing Journal 33, 102872. doi:10.1520/GTJ102872.

Arulnathan, R., Boulanger, R.W., Riemer, M.F., 1998. Analysis of Bender Element Tests. Geotechnical Testing Journal 21, 120–131. doi:10.1520/GTJ10750J.

Astuto, G., Molina-Gómez, F., Bilotta, E., Viana da Fonseca, A., Flora, A., 2022. Some remarks on the assessment of P-wave velocity in laboratory tests for evaluating the degree of saturation. Acta Geotechnica doi:10.1007/s11440-022-01610-9.

Barrière, J., Bordes, C., Brito, D., Sénéchal, P., Perroud, H., 2012. Labora-

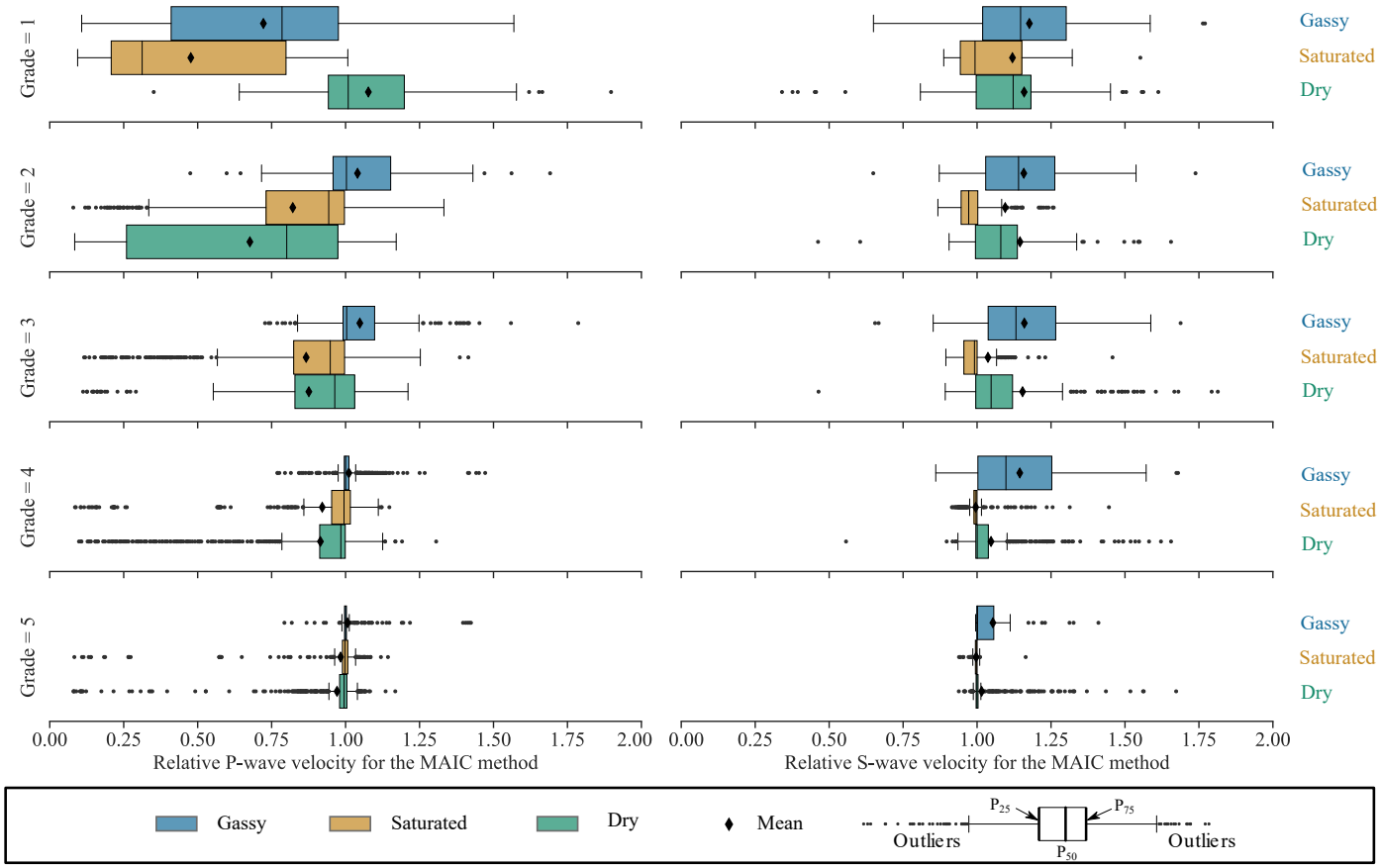

Figure 17: Ratio between the velocity determined using the *MAIC* algorithm and the manual *Start-to-Start* method. Values greater than one indicate that *MAIC* is overestimating the velocity and correspond to positive values of relative deviation.

tory monitoring of P waves in partially saturated sand. Geophysical Journal International doi:10.1111/j.1365-246X.2012.05691.x.

Bialowas, G.A., Diambra, A., Nash, D.F.T., 2018. Stress and time-dependent properties of crushed chalk. Proceedings of the Institution of Civil Engineers - Geotechnical Engineering 171, 530–544. doi:10.1680/jgeen.17.00168.

Blewett, J., Blewett, I.J., Woodward, P.K., 1999. Measurement of shear-wave velocity using phase-sensitive detection techniques. Canadian Geotechnical Journal 36, 934–939.

Blewett, J., Blewett, I.J., Woodward, P.K., 2000. Phase and amplitude responses associated with the measurement of shear-wave velocity in sand by bender elements. Canadian Geotechnical Journal 37, 1348–1357. doi:10.1139/t00-047.

Bonal, J., Donohue, S., McNALLY, C., 2012. Wavelet analysis of bender element signals. Géotechnique 62, 243–252. doi:10.1680/geot.9.P.052.

Brignoli, E.G., Gotti, M., Stokoe, K.H., 1996. Measurement of shear waves in laboratory specimens by means of piezoelectric transducers. Geotechnical Testing Journal 19, 384–397.

Cai, Y., Dong, Q., Wang, J., Gu, C., Xu, C., 2015. Measurement of small strain shear modulus of clean and natural sands in saturated condition using bender element test. Soil Dynamics and Earthquake Engineering 76, 100–110. doi:10.1016/j.soildyn.2014.12.013.

Camacho-Tauta, J., Ferreira, C., Santos, J., Viana da Fonseca, A., 2008. Moving windows algorithm to reduce uncertainties in bender element testing .

Camacho-Tauta, J.F., Cascante, G., Viana Da Fonseca, A., Santos, J.A., 2015. Time and frequency domain evaluation of bender element systems. Géotechnique 65, 548–562. doi:10.1680/geot.13.P.206.

Chen, G., Wang, F.T., Li, D.Q., Liu, Y., 2020. Dyadic wavelet analysis of bender element signals in determining shear wave velocity. Canadian Geotechnical Journal 57, 2027–2030. doi:10.1139/cgj-2019-0167.

Delfosse-Ribay, E., Djeran-Maigre, I., Cabrillac, R., Gouvenot, D., 2004. Shear modulus and damping ratio of grouted sand. Soil Dynamics and Earthquake Engineering 24, 461–471. doi:10.1016/j.soildyn.2004.02.004.

Dyvik, R., Madshus, C., 1985. Lab Measurements of Gmax Using Bender Elements, in: Advances in the Art of Testing Soils Under Cyclic Conditions, ASCE. pp. 186–196.

Ferreira, C., Martins, J.P., Gomes Correia, A., 2013. Determination of the Small-Strain Stiffness of Hard Soils by Means of Bender Elements and Accelerometers. Geotechnical and Geological Engineering 32, 1369–1375. doi:10.1007/s10706-013-9678-7.

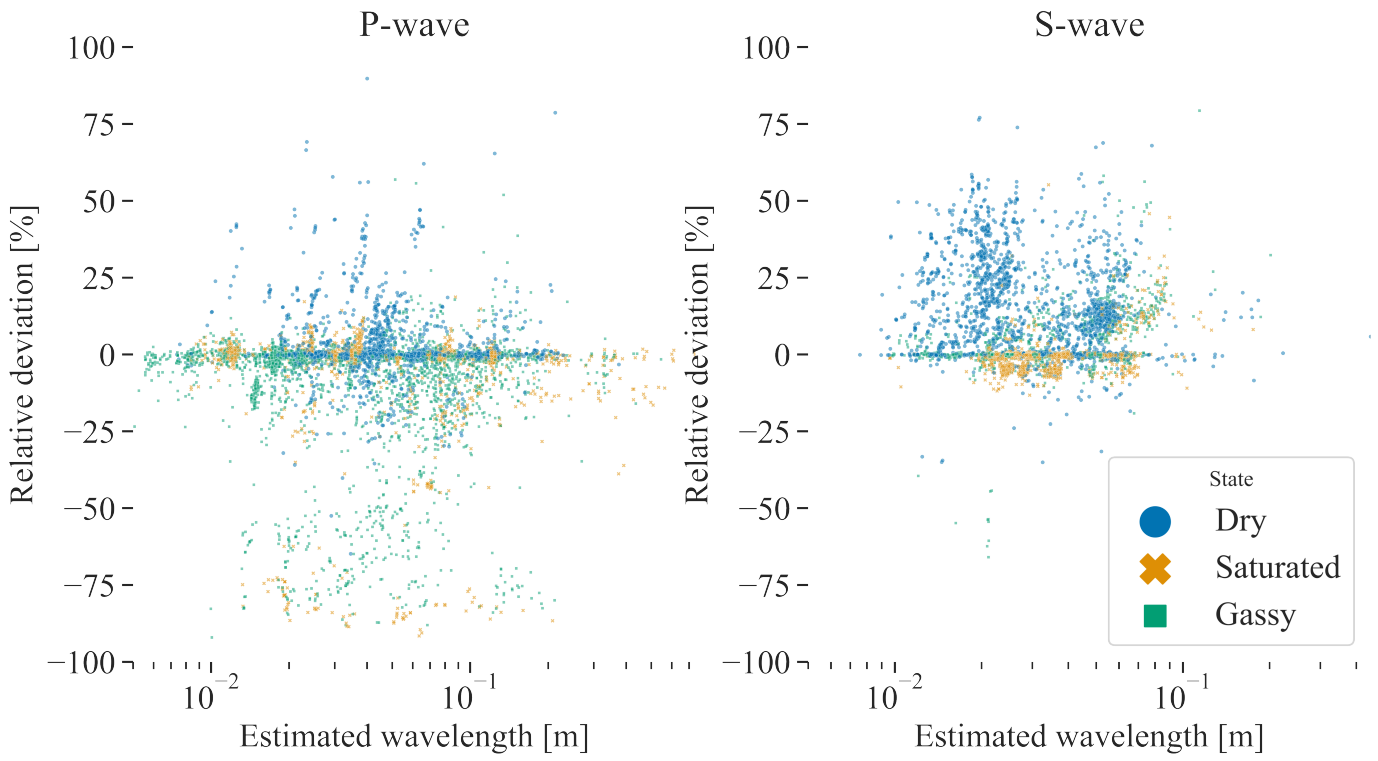

Figure 18: Effect of wavelength on observed relative deviation between manual and *MAIC* interpretations. All signals shown here were recorded using a specimens 0.2 m long. Therefore, far-field conditions could be satisfied for wavelengths below 0.1 m.

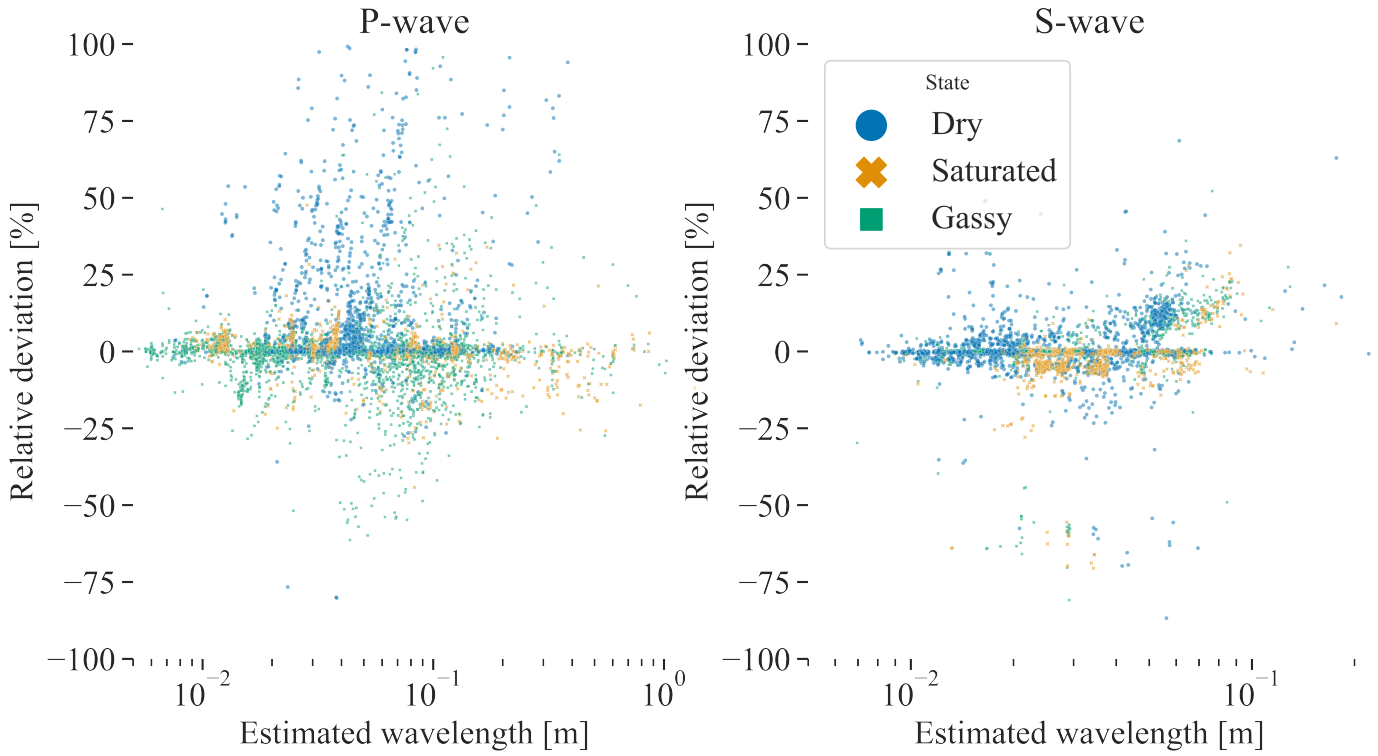

Figure 19: Effect of wavelength on observed relative deviation between manual and *SLA* interpretations. All signals shown here were recorded using a specimens 0.2 m long. Therefore, far-field conditions could be satisfied for wavelengths below 0.1 m.

Finas, M., Vanheeghe, P., Ali, H., Cascante, G., 2016. Automatic Shear Wave Velocity Estimation in Bender Element Testing. Geotechnical Testing Journal 39, 557–567. doi:10.1520/GTJ20140197.

Flood-Page, G., Boutonnier, L., Pereira, J.M., 2023. Relating wave frequency and pore fluid homogeneity in quasi-saturated sands. E3S Web of Conferences 382, 03005. doi:10.1051/e3sconf/202338203005.

Goudarzy, M., König, D., Schanz, T., 2018. Interpretation of small and intermediate strain characteristics of Hostun sand for various stress states. Soils and Foundations 58, 1526–1537. doi:10.1016/j.sandf.2018.09.002.

Greening, P., Rio, J., Arroyo, M., 2007. Some observations from a parametric study of the behaviour of benders in a polyurethane rubber , 8.

Greening, P.D., Nash, D.F., 2004. Frequency Domain Determination of G0 Using Bender Elements. Geotechnical Testing Journal 27, 11192. doi:10.1520/GTJ11192.

Gu, X., Yang, J., Huang, M., 2013. Laboratory measurements of small strain properties of dry sands by bender element. Soils and Foundations 53, 735–745. doi:10.1016/j.sandf.2013.08.011.

Hasan, A.M., Wheeler, S.J., 2015. Measuring travel time in bender/extender element tests, in: Proceedings of the XVI ECSMGE Geotechnical Engineering for Infrastructure and Development, ICE. doi:doi:10.1680/ecsmge.60678.

Jovičić, V., Coop, M.R., Simić, M., 1996. Objective criteria for determining Gmax from bender element tests. Géotechnique 46, 357–362. doi:10.1680/geot.1996.46.2.357.

Kawaguchi, T., Mitachi, T., Shibuya, S., 2001. Evaluation of shear wave travel time in laboratory bender element test, in: International Conference on Soil Mechanics and Geotechnical Engineering, pp. 155–158.

Kumar, J., Shinde, N.S., 2019. Interpretation of bender element test results using sliding Fourier transform method. Canadian Geotechnical Journal 56, 2004–2014. doi:10.1139/cgj-2018-0733.

Lawrence Jr, F.V., 1965. Ultrasonic Shear Wave Velocities in Sand and Clay. Technical Report. Massachusetts Inst of Technology, Cambridge, Department of civil engineering.

Lee, J.S., Santamarina, J.C., 2005. Bender Elements: Performance and Signal Interpretation. Journal of Geotechnical and Geoenvironmental Engineering 131, 1063–1070. doi:10.1061/(ASCE)1090-0241(2005)131:9(1063).

Leong, E.C., Cahyadi, J., Rahardjo, H., 2009. Measuring shear and compression wave velocities of soil using bender–extender elements. Canadian Geotechnical Journal 46, 792–812. doi:10.1139/T09-026.

Leong, E.C., Yeo, S.H., Rahardjo, H., 2005. Measuring Shear Wave Velocity Using Bender Elements. Geotechnical Testing Journal 28, 488–498. doi:10.1520/GTJ12196.

Lings, M.L., Greening, P.D., 2001. A novel bender/extender element for soil testing. Géotechnique 51, 713–717. doi:10.1680/geot.2001.51.8.713.

Menq, F.Y., 2003. Dynamic Properties of Sandy and Gravelly Soils. Ph.D. thesis. The University of Texas. Austin.

Myung, I.J., 2003. Tutorial on maximum likelihood estimation. Journal of Mathematical Psychology 47, 90–100. doi:10.1016/S0022-2496(02)00028-7.

Nakagawa, K., Soga, K., Mitchell, J.K., 1997. Observation of Biot compressional wave of the second kind in granular soils. Géotechnique 47, 133–147. doi:10.1680/geot.1997.47.1.133.

Nash, D., Sukolrat, J., Greening, P., Benahmed, N., 2007. Comparison of shear wave velocity measurements in a soft clay specimen using time and frequency domain techniques. Rivista Italiana di Geotecnica 25, 56–68.

Nicholson, J.M., Mordaunt, M., Lopez, P., Uppala, A., Rosati, D., Rodrigues, N.P., Grabitz, P., Rife, S.C., 2021. Scite: A smart citation index that displays the context of citations and classifies their intent using deep learning. Quantitative Science Studies 2, 882–898.

O'Donovan, J., O'Sullivan, C., Marketos, G., 2012. Two-dimensional discrete element modelling of bender element tests on an idealised granular material. Granular Matter 14, 733–747. doi:10.1007/s10035-012-0373-9.

O'Donovan, J., O'sullivan, C., Marketos, G., Wood, D.M., 2015. Analysis of bender element test interpretation using the discrete element method. Granular Matter 17, 197–216.

Rio, JFME., 2006. Advances in Laboratory Geophysics Using Bender Elements. Ph.D. thesis. University College London. London, United Kingdom.

Sanchez-Salinero, I., Roesset, J.M., Stokoe, I.I., Kenneth, H., 1986. Analytical Studies of Body Wave Propagation and Attenuation. Technical Report. Texas Univ At Austin Geotechnical Engineering Center.

Santamarina, J.C., Klein, K.A., Fam, M.A., 2001. Soils and Waves. volume 316. J. Wiley & Sons New York.

Shirley, D.J., Hampton, L.D., 1978. Shear-wave measurements in laboratory sediments. The Journal of the Acoustical Society of America 63, 607–613. doi:10.1121/1.381760.

Sleeman, R., van Eck, T., 1999. Robust automatic P-phase picking: An online implementation in the analysis of broadband seismogram recordings. Physics of the Earth and Planetary Interiors 113, 265–275. doi:10.1016/S0031-9201(99)00007-2.

Souto, A., Hartikainen, J., Özüdo˘gru, K., 1994. Measurement of dynamic parameters of road pavement materials by the bender element and resonant column tests. Géotechnique 44, 519–526. doi:10.1680/geot.1994.44.3.519.

Subramaniyan, S., Quintal, B., Madonna, C., Saenger, E.H., 2015. Laboratory-based seismic attenuation in Fontainebleau sandstone: Evidence of squirt flow. Journal of Geophysical Research: Solid Earth 120, 7526–7535. doi:10.1002/2015JB012290.

Tatsuoka, F., Iwasaki, T., Yoshida, S., Fukushima, S., Sudo, H., 1979. Shear Modulus and Damping by Drained tests on Clean Sand Specimens Reconstituted by Various Methods. Soils and Foundations 19, 39–54. doi:10.3208/sandf1972.19.39.

Vaezi, Y., van der Baan, M., 2015. Comparison of the STA/LTA and power spectral density methods for microseismic event detection. Geophysical Journal International 203, 1896–1908. doi:10.1093/gji/ggv419.

Valle-Molina, C., 2006. Measurements of Vp and Vs in Dry, Unsaturated and Saturated Sand Specimens with Piezoelectric Transducers. Ph.D. thesis. The

University of Texas at Austin.

Valle-Molina, C., Stokoe, K.H., 2012. Seismic measurements in sand specimens with varying degrees of saturation using piezoelectric transducers. Canadian Geotechnical Journal 49, 671–685. doi:10.1139/t2012-033.

Viana da Fonseca, A., Ferreira, C., Fahey, M., 2009. A Framework Interpreting Bender Element Tests, Combining Time-Domain and Frequency-Domain Methods. Geotechnical Testing Journal 32, 100974. doi:10.1520/GTJ100974.

Viggiani, G., Atkinson, J.H., 1995. Interpretation of bender element tests. Geotechnique 45, 149–154.

Vilhar, G., Jovičić, V., 2009. Measurement and interpretation of the small strain stifness of Boštanj silty sand. Acta Geotechnica Slovenica 6, 57–75.

Virtanen, P., Gommers, R., Oliphant, T.E., Haberland, M., Reddy, T., Cournapeau, D., Burovski, E., Peterson, P., Weckesser, W., Bright, J., van der Walt, S.J., Brett, M., Wilson, J., Millman, K.J., Mayorov, N., Nelson, A.R.J., Jones, E., Kern, R., Larson, E., Carey, C.J., Polat, İ., Feng, Y., Moore, E.W., VanderPlas, J., Laxalde, D., Perktold, J., Cimrman, R., Henriksen, I., Quintero, E.A., Harris, C.R., Archibald, A.M., Ribeiro, A.H., Pedregosa, F., van Mulbregt, P., 2020. SciPy 1.0: Fundamental algorithms for scientific computing in Python. Nature Methods 17, 261–272. doi:10.1038/s41592-019-0686-2.

Wang, Y., Benahmed, N., Cui, Y.J., Tang, A.M., 2017. A novel method for determining the small-strain shear modulus of soil using the bender elements technique. Canadian Geotechnical Journal 54, 280–289. doi:10.1139/cgj-2016-0341.

Whalley, W.R., Jenkins, M., Attenborough, K., 2011. The Velocity of Shear Waves in Saturated Soil. Soil Science Society of America Journal 75, 1652–1657. doi:10.2136/sssaj2010.0449.

Wichtmann, T., Triantafyllidis, T., 2010. On the influence of the grain size distribution curve on P-wave velocity, constrained elastic modulus Mmax and Poisson's ratio of quartz sands. Soil Dynamics and Earthquake Engineering 30, 757–766. doi:10.1016/j.soildyn.2010.03.006.

Yamashita, S., Kawaguchi, T., Nakata, Y., Mikami, T., Fujiwara, T., Shibuya, S., 2009. Interpretation of International Parallel Test on the Measurement of Gmax Using Bender Elements. Soils and Foundations 49, 631–650. doi:10.3208/sandf.49.631.

Zhang, H., Thurber, C., Rowe, C., 2003. Automatic P-wave arrival detection and picking with multiscale wavelet analysis for single-component recordings. Bulletin of the Seismological Society of America 93, 1904–1912.

Zhang, Z., Wang, Y.H., 2014. The use of P-wave velocity tomography–a particular application on exploring the mechanism of friction fatigue, in: International Symposium on Geomechanics from Micro to Macro (IS-Cambridge), Cambridge, United Kingdom, CRC Press, Boca Raton, FL, pp. 1165–1170.

Wave	State	Grade	$\bar{x}$	σ	P_1	P_5	P_{25}	P_{50}	P_{75}	P_{95}	P_{99}
P	Dry	1	19.01	65.5	-100.45	-100.34	-5.02	5.31	45.21	128.78	211.11
P	Dry	2	-3.68	44.36	-100.43	-100.36	-10.37	1.29	15.29	51.89	90.37
P	Dry	3	-0.86	40.25	-100.38	-100.31	-0.9	1.22	14.84	42.31	108.28
P	Dry	4	3.82	21.29	-100.29	-1.11	-0.01	0.5	3.21	33.64	73.4
P	Dry	5	8.33	21.87	-1.76	-0.47	-0.03	0.44	3.02	47.63	98.04
P	Saturated	1	3.79	14.36	-27.64	-19.2	-1.11	1.91	8.26	28.07	31.21
P	Saturated	2	-3.87	15.31	-33.98	-27.63	-15.17	-1.46	4.7	21.89	28.33
P	Saturated	3	-0.27	11.49	-23.01	-18.6	-10.58	0.17	7.22	18.55	26.72
P	Saturated	4	1.68	7.36	-19.54	-10.9	-0.75	1.19	4.44	12.15	25.41
P	Saturated	5	0.96	3.03	-4.44	-1.98	-0.3	0.49	1.63	5.93	12.61
P	Gassy	1	6.75	33.43	-48.16	-29.19	-9.46	0.44	15.82	58.55	136.46
P	Gassy	2	2.55	24.24	-39.37	-23.99	-5.16	-0.06	4.59	34.43	120.38
P	Gassy	3	-0.31	14.98	-39.11	-20.05	-5.87	-0.21	2.75	20.75	43.98
P	Gassy	4	-0.32	8.93	-23.89	-12.81	-1.87	-0.15	1.55	11.87	23.9
P	Gassy	5	0.81	4.09	-12.65	-4.24	-0.61	0.39	2.01	7.42	13.53
S	Dry	1	0.92	22.87	-70.08	-36.54	-2.19	1.64	14.25	28.31	48.74
S	Dry	2	1.48	16.59	-87.31	-11.97	-3.18	-0.09	5.52	26.46	36.73
S	Dry	3	0.29	9.87	-53.53	-7.27	-1.54	-0.13	1.64	12.16	31.66
S	Dry	4	0.34	3.81	-3.1	-2.04	-0.51	-0.18	0.03	4.19	18.54
S	Dry	5	0.09	1.83	-1.01	-0.75	-0.38	-0.22	-0.02	0.24	7.13
S	Saturated	1	7.13	38.88	-87.89	-60.01	-6.14	10.94	19.87	54.56	122.34
S	Saturated	2	-0.37	38.59	-100.48	-67.82	-4.87	-0.63	1.86	25.91	131.35
S	Saturated	3	-5.13	17.25	-100.37	-24.14	-5.18	-1.17	-0.16	8.31	14.01
S	Saturated	4	-0.61	4.48	-8.09	-4.24	-0.76	-0.17	0.15	1.17	13.17
S	Saturated	5	-0.4	4.32	-2.26	-1.23	-0.27	-0.05	0.16	0.56	1.03
S	Gassy	1	9.03	37.39	-97.55	-61.01	0.47	12.5	17.6	54.44	93.2
S	Gassy	2	5.43	31.08	-100.49	-55.41	-0.84	6.59	13.3	49.54	123.29
S	Gassy	3	1.3	21.03	-100.36	-6.26	-1.27	-0.06	6.1	26.05	59.54
S	Gassy	4	-0.11	7.92	-9.73	-1.9	-0.51	-0.1	0.27	5.5	18.41
S	Gassy	5	-0.33	4.56	-2.29	-1.21	-0.29	-0.03	0.22	0.8	3.48

Table 6: Relative deviation associated with the *SLA* method for different grades and saturation states. P_n indicates the n^{th} percentile of the statistical distribution.

Wave	State	Grade	$\bar{x}$	σ	P_1	P_5	P_{25}	P_{50}	P_{75}	P_{95}	P_{99}
P	Dry	1	7.7	24.45	-35.01	-25.09	-5.83	0.89	19.85	46.47	84.16
P	Dry	2	4.04	17.78	-36.31	-25.99	-4.23	0.29	15.25	37.75	48.51
P	Dry	3	4.82	15.03	-21.77	-13.57	-0.86	0.37	9.82	26.19	42.61
P	Dry	4	1.12	6.1	-15.35	-3.7	-0.45	-0.0	1.14	9.83	23.81
P	Dry	5	0.64	4.93	-6.68	-0.89	-0.35	-0.04	0.3	3.74	22.67
P	Saturated	1	-52.32	31.99	-89.24	-83.88	-79.23	-68.76	-20.13	-0.88	0.43
P	Saturated	2	-32.35	34.08	-88.32	-84.71	-74.06	-19.89	-2.6	8.11	14.58
P	Saturated	3	-12.42	25.09	-87.14	-82.54	-17.13	-3.65	3.07	11.46	17.21
P	Saturated	4	-7.89	21.89	-87.83	-78.2	-4.71	-0.53	1.62	7.12	11.06
P	Saturated	5	-1.69	10.45	-73.27	-4.0	-1.07	-0.21	0.72	3.04	6.48
P	Gassy	1	-27.79	32.8	-85.78	-79.24	-58.97	-21.48	-2.44	16.66	53.11
P	Gassy	2	-17.85	26.65	-84.32	-75.23	-26.87	-5.7	-0.39	11.65	18.75
P	Gassy	3	-13.33	22.27	-81.93	-65.77	-17.54	-5.18	-0.34	7.35	16.68
P	Gassy	4	-8.51	18.46	-83.95	-59.23	-8.75	-1.6	-0.11	3.14	8.44
P	Gassy	5	-2.89	11.42	-78.44	-14.11	-2.02	-0.5	0.42	2.51	5.45
S	Dry	1	17.68	20.34	-29.06	-14.09	1.89	14.71	30.14	54.6	70.46
S	Dry	2	15.8	15.42	-9.83	-5.18	2.91	14.02	26.28	45.7	53.57
S	Dry	3	15.98	14.81	-11.51	-1.64	3.74	13.15	26.58	42.38	53.74
S	Dry	4	14.43	15.69	-1.89	-0.58	0.27	9.76	25.26	43.98	53.83
S	Dry	5	5.35	10.01	-0.46	-0.42	-0.05	0.15	5.65	29.18	37.25
S	Saturated	1	11.96	40.6	-10.41	-7.59	-5.67	-0.69	15.13	35.63	220.11
S	Saturated	2	9.51	57.35	-11.51	-8.41	-5.39	-2.84	0.25	23.45	345.87
S	Saturated	3	3.68	37.8	-9.48	-6.72	-4.46	-0.88	0.02	11.41	242.4
S	Saturated	4	-0.46	4.03	-6.99	-5.71	-1.02	-0.37	-0.0	1.13	17.56
S	Saturated	5	-0.32	1.2	-4.72	-1.49	-0.57	-0.22	0.02	0.49	0.9
S	Gassy	1	15.91	43.82	-62.02	-19.16	-0.3	12.2	18.21	55.68	234.74
S	Gassy	2	14.51	38.13	-25.99	-6.46	-0.55	8.02	13.62	54.64	208.74
S	Gassy	3	15.38	42.45	-7.83	-4.76	-0.43	4.75	12.0	55.35	260.97
S	Gassy	4	4.72	16.48	-5.52	-1.62	-0.43	0.05	3.8	23.85	54.41
S	Gassy	5	1.55	6.6	-1.87	-1.12	-0.33	-0.04	0.34	12.02	32.4

Table 7: Relative deviation associated with the *MAIC* method for different grades and saturation states.

Wave	State	Grade	$\bar{x}$	σ	P_1	P_5	P_{25}	P_{50}	P_{75}	P_{95}	P_{99}
P	Dry	1	1.39	0.45	0.76	0.86	1.0	1.39	1.57	2.19	2.98
P	Dry	2	1.25	0.3	0.74	0.87	1.0	1.2	1.43	1.82	1.95
P	Dry	3	1.17	0.25	0.84	0.95	1.0	1.09	1.24	1.72	2.09
P	Dry	4	1.05	0.16	0.96	0.99	1.0	1.01	1.05	1.28	1.83
P	Dry	5	1.04	0.16	0.99	1.0	1.0	1.0	1.01	1.3	1.85
P	Saturated	1	1.03	0.14	0.73	0.82	0.97	1.01	1.07	1.28	1.31
P	Saturated	2	0.96	0.16	0.66	0.73	0.85	0.99	1.05	1.26	1.29
P	Saturated	3	1.0	0.11	0.77	0.82	0.92	1.0	1.07	1.19	1.27
P	Saturated	4	1.01	0.07	0.81	0.89	0.99	1.01	1.03	1.1	1.25
P	Saturated	5	1.01	0.03	0.96	0.98	1.0	1.0	1.01	1.04	1.08
P	Gassy	1	1.05	0.34	0.45	0.67	0.89	1.0	1.14	1.61	2.32
P	Gassy	2	1.02	0.25	0.54	0.75	0.95	1.0	1.04	1.34	2.2
P	Gassy	3	0.99	0.15	0.58	0.8	0.94	1.0	1.02	1.21	1.44
P	Gassy	4	0.99	0.09	0.76	0.87	0.98	1.0	1.01	1.07	1.24
P	Gassy	5	1.0	0.04	0.87	0.96	0.99	1.0	1.01	1.05	1.1
S	Dry	1	1.01	0.23	0.32	0.43	0.97	1.01	1.12	1.32	1.49
S	Dry	2	1.03	0.12	0.81	0.9	0.98	1.0	1.07	1.26	1.36
S	Dry	3	1.02	0.08	0.81	0.93	0.99	1.0	1.05	1.14	1.28
S	Dry	4	1.01	0.04	0.94	0.98	1.0	1.0	1.0	1.08	1.18
S	Dry	5	1.0	0.02	0.99	0.99	1.0	1.0	1.0	1.0	1.08
S	Saturated	1	0.99	0.29	0.31	0.37	0.94	0.96	1.12	1.26	2.02
S	Saturated	2	1.0	0.21	0.61	0.86	0.94	0.96	1.0	1.22	2.3
S	Saturated	3	0.97	0.07	0.76	0.91	0.95	0.97	1.0	1.05	1.12
S	Saturated	4	0.99	0.03	0.92	0.94	0.99	1.0	1.0	1.01	1.03
S	Saturated	5	1.0	0.03	0.98	0.99	1.0	1.0	1.0	1.01	1.01
S	Gassy	1	1.1	0.34	0.31	0.43	1.0	1.12	1.17	1.54	1.93
S	Gassy	2	1.08	0.25	0.43	0.91	0.99	1.07	1.13	1.49	2.23
S	Gassy	3	1.03	0.15	0.41	0.94	0.99	1.0	1.06	1.22	1.59
S	Gassy	4	1.0	0.05	0.94	0.98	1.0	1.0	1.0	1.06	1.18
S	Gassy	5	1.0	0.04	0.98	0.99	1.0	1.0	1.0	1.01	1.03

Table 8: Relative velocity for the *SLA* method for different grades and saturation states

Wave	State	Grade	$\bar{x}$	σ	P_1	P_5	P_{25}	P_{50}	P_{75}	P_{95}	P_{99}
P	Dry	1	1.08	0.24	0.65	0.75	0.94	1.01	1.2	1.46	1.84
P	Dry	2	1.04	0.18	0.64	0.74	0.96	1.0	1.15	1.38	1.49
P	Dry	3	1.05	0.15	0.78	0.86	0.99	1.0	1.1	1.26	1.43
P	Dry	4	1.01	0.06	0.85	0.96	1.0	1.0	1.01	1.1	1.24
P	Dry	5	1.01	0.05	0.93	0.99	1.0	1.0	1.0	1.04	1.23
P	Saturated	1	0.48	0.32	0.11	0.16	0.21	0.31	0.8	0.99	1.0
P	Saturated	2	0.68	0.34	0.12	0.15	0.26	0.8	0.97	1.08	1.15
P	Saturated	3	0.88	0.25	0.13	0.17	0.83	0.96	1.03	1.11	1.17
P	Saturated	4	0.92	0.22	0.12	0.22	0.95	0.99	1.02	1.07	1.11
P	Saturated	5	0.98	0.1	0.27	0.96	0.99	1.0	1.01	1.03	1.06
P	Gassy	1	0.72	0.33	0.14	0.21	0.41	0.79	0.98	1.17	1.53
P	Gassy	2	0.82	0.27	0.16	0.25	0.73	0.94	1.0	1.12	1.19
P	Gassy	3	0.87	0.22	0.18	0.34	0.82	0.95	1.0	1.07	1.17
P	Gassy	4	0.91	0.18	0.16	0.41	0.91	0.98	1.0	1.03	1.08
P	Gassy	5	0.97	0.11	0.22	0.86	0.98	0.99	1.0	1.03	1.05
S	Dry	1	1.18	0.2	0.71	0.86	1.02	1.15	1.3	1.55	1.7
S	Dry	2	1.16	0.15	0.9	0.95	1.03	1.14	1.26	1.46	1.54
S	Dry	3	1.16	0.15	0.88	0.98	1.04	1.13	1.27	1.42	1.54
S	Dry	4	1.14	0.16	0.98	0.99	1.0	1.1	1.25	1.44	1.54
S	Dry	5	1.05	0.1	1.0	1.0	1.0	1.0	1.06	1.29	1.37
S	Saturated	1	1.12	0.41	0.9	0.92	0.94	0.99	1.15	1.36	3.2
S	Saturated	2	1.1	0.57	0.88	0.92	0.95	0.97	1.0	1.23	4.46
S	Saturated	3	1.04	0.38	0.91	0.93	0.96	0.99	1.0	1.11	3.42
S	Saturated	4	1.0	0.04	0.93	0.94	0.99	1.0	1.0	1.01	1.18
S	Saturated	5	1.0	0.01	0.95	0.99	0.99	1.0	1.0	1.0	1.01
S	Gassy	1	1.16	0.44	0.38	0.81	1.0	1.12	1.18	1.56	3.35
S	Gassy	2	1.15	0.38	0.74	0.94	0.99	1.08	1.14	1.55	3.09
S	Gassy	3	1.15	0.42	0.92	0.95	1.0	1.05	1.12	1.55	3.61
S	Gassy	4	1.05	0.16	0.94	0.98	1.0	1.0	1.04	1.24	1.54
S	Gassy	5	1.02	0.07	0.98	0.99	1.0	1.0	1.0	1.12	1.32

Table 9: Relative velocity for the *MAIC* method for different grades and saturation states.